Applied Energy 208 (2017) 1318–1342

Contents lists available at ScienceDirect

Applied Energy

journal homepage: www.elsevier.com/locate/apenergy

Thermionic energy conversion for concentrating solar power

Gang Xiao[a], Guanghua Zheng[a], Min Qiu[b], Qiang Li[b], Dongsheng Li[c], Mingjiang Ni[a,*]

[a] State Key Laboratory of Clean Energy Utilization, Zhejiang University, Hangzhou 310027, China
[b] State Key Laboratory of Modern Optical Instrumentation, Zhejiang University, Hangzhou 310027, China
[c] State Key Laboratory of Silicon Materials, Zhejiang University, Hangzhou 310027, China

HIGHLIGHTS

- Methods is outlined to improve the efficiency of heat-induced solar thermionic converter.
- Optimization of materials and structure is summarized for photon-enhanced thermionic converter.
- Combined systems with thermionic energy converters is proposed for concentrating solar power.
- Roadmap of thermionic energy conversion for concentrating solar power is brought forward.

ARTICLE INFO

Keywords:
Concentrating solar power (CSP)
Thermionics
Heat-induced
Photon-enhanced
Thermodynamic analysis

ABSTRACT

Concentrating solar power (CSP) is a mainstream of solar energy utilization, and thermionic emission is a potential way to convert concentrated solar radiation into power with a theoretical efficiency of 50–70%, surpassing both Shockley-Queisser limit and photo-thermal limit. This literature attempts to provide a comprehensive understanding of and an insight into solar thermionic energy conversion. The fundamentals of electron emission from electrodes and electron transport in vacuum gap are presented, as well as the state of the art of solar thermionic energy conversion technologies, including heat-induced thermionics and photon-enhanced thermionics. The former is driven by thermal energy, whereas the latter takes advantage of both quantum photon energy and thermal energy. Burgeoning research indicates that photon-enhanced thermionic conversion is a promising technology for concentrating solar power due to the high efficiency and simple operating mode. Now, it is important to develop novel materials and coating technologies to facilitate electron emission and reduce space charge effect in interelectrode vacuum. Structural design of thermionic converters and top–bottom configuration of solar-electricity systems are suggested for practical applications.

1. Introduction

Solar energy, the primary and most abundant carbon–neutral energy source, has attracted progressively more attention due to the growing energy demand and the environmental pollution. It is reported by the International Energy Agency that solar power will provide 27% of the world's electricity and replace fossil fuels to become the leading energy source by 2050 [1,2]. Normally, solar power can be divided into non-concentrating and concentrating modes (CSP). The non-concentrating solar power system, i.e., flat-plate photovoltaics (PV), can collect and convert both direct and diffuse solar radiation into electricity [3]. However, the intensity of solar radiation is low on the earth (usually less than 1000 W/m^2) and thus a large amount of costly solar cells is required. The concentrating PV, which employs reflective mirrors (or refractive optical lenses) to focus sunlight onto solar cells, can reduce the amount of required solar cells and enhance the solar-to-electric efficiency simultaneously [4,5]. However, thermal management should be considered to ensure rated power output and lifetime of concentrating PV cells [6]. Another technical route for concentrating solar power is solar-thermal conversion, which can be integrated with thermal storage and mainly includes solar thermal power [7,8], thermoelectric energy generation [9] and thermionic energy conversion [10]. Concentrating solar thermal power, a method of using heat collected by a solar concentrator to drive a heat engine to generate electricity, is mainly limited by the heat transfer capacity of working fluid and mechanical losses. Thermoelectric generators can convert solar radiation to electricity via Seebeck effect, which depends on the temperature difference between the heat source and heat sink. However, they usually suffer from intrinsic limitation of the material properties, such as the reciprocal relationship between the Seebeck coefficient and

* Corresponding author.
E-mail address: ceu_ni@zju.edu.cn (M. Ni).

http://dx.doi.org/10.1016/j.apenergy.2017.09.021
Received 23 May 2017; Received in revised form 27 August 2017; Accepted 7 September 2017
Available online 15 September 2017

Nomenclature

A	richardson constant of the emitter
B	radiative recombination coefficient
C_n	auger recombination coefficient for electrons
C_p	auger recombination coefficient for holes
D	electron diffusion coefficient
d	thickness of emitter
dn	non-equilibrium electron concentration
E_C	conduction band minimum of the material
E_F	fermi level of the emitter
E'_F	fermi level of the collector
$E_{F,n}$	quasi-fermi level of the emitter
E_g	energy bandgap of the emitter
E_V	valence band minimum of the emitter
E_{vacuum}	vacuum level of the emitter
E'_{vacuum}	vacuum level of the collector
f	distribution function of electrons
G	rate of photoexcitation of conduction band electrons
h	planck constant
J	total current output
J_{em}	current density from emitter
J'_{em}	photon-enhanced thermionic current density
J_{PE}	photoemission current density
J_{rev}	reverse current density from collector
k	Boltzmann's constant
L	electron diffusion length
l	perpendicular distance from the emissive surface in the bulk material
m_e	electron mass
m_e^*	electron effective mass
N	electron number density in the interelectrode gap
n	total conduction band population
n_{eq}	equilibrium electron concentration
P_{PETE}	power output of photon-enhanced thermionic emission
P_{sun}	total input power of solar radiation
P_{TE}	power output of heat-induced thermionic emission
p	density of holes
Q	waste heat from thermionic energy converter
q	electron charge
S_{back}	recombination velocity at the back surface
$S_{emission}$	emission velocity
$S_{recombination}$	surface recombination velocity
T_C	temperature of collector
T_E	temperature of emitter
v_0	initial velocity of electron in the direction normal to the surface
v_x	velocity component of electron in the direction normal to the surface
v_y	one velocity component of electron parallel to the surface
v_z	one velocity component of electron parallel to the surface
V	output voltage of TEC
V_C	voltage output at the critical point
V_S	voltage output at the saturation point
X	concentration ratio
x	perpendicular distance from the emissive surface in the interelectrode
x_m	perpendicular distance of maximum motive

Greek symbols

υ	frequency of photon
ϕ	electron motive
ϕ_C	work function of collector
ϕ_E	work function of emitter
ϕ_m	maximum electron motive in the interelectrode
χ	electron affinity of emitter
η_{TE}	conversion efficiency of heat-induced thermionic emission
η_{PETE}	conversion efficiency of photon-enhanced thermionic emission
τ_{bulk}	bulk recombination lifetime
τ_n	total minority electron lifetime in the bulk
τ_{SRH}	Shockley-Read-Hall (SRH) recombination lifetime
ζ	a dimensionless reduced rate of surface recombination at the back surface
ε_0	permittivity of vacuum
Γ_{sun}	photogeneration rate of the conduction band electrons
Γ_{PETE}	rate of photon-enhanced thermionic emission
$\Gamma_{recombination}$	rate of electron recombination
ΔS	entropy production

Abbreviations

CNTs	carbon nanotubes
CSP	concentrating solar power
HITE	heat-induced thermionic emission
NEA	negative electron affinity
PETE	photon-enhanced thermionic emission
PV	photovoltaics
TEC	thermionic energy converter

electrical conductivity. Thermionic energy converter (TEC), which uses electrons as working fluid and vacuum as the active electron transport channel, is a rising candidate for concentrating solar power.

The overall historical progress on solar thermionic energy conversion is summarized [14–25], as shown in Fig. 1. Solar thermionics have attracted intensive studies since the first experimental demonstration of thermionic energy conversion in the 1950s [11]. The first concentrating solar thermionic prototype sponsored by the Solar Energy Thermionic Program for space missions achieved an efficiency of 4–7%, which is considerably lower than the theoretical conversion efficiency (over 60%) under ideal conditions [12]. There exists a large gap between promising theoretical efficiency and inadequate real efficiency, usually due to the tradeoff between work function and operating temperature. The non-ideal efficiency and high cost hinder the development of solar thermionics. In recent years, however, the renaissance of thermionic energy conversion has been observed due to the development of microtechnology and nanotechnology. General Atomics Inc. proposed a High Power Advanced Low Mass (HPALM) solar thermionics space power system that would deliver outputs on the order of 50 kW_e [13]. The advanced carbon nanomaterials have joined and played an increasing roles for the development of solar thermionic energy conversion. On the other hand, Smestad firstly discovered a combined photoelectric-thermionic effect using a heated vacuum photodiode [14]. Later, in 2010, an innovative thermionic conversion mechanism called photon-enhanced thermionic emission (PETE) was put forward, which exhibits a theoretical efficiency of 43% alone and 52.9% when combined with bottoming thermal cycle [15]. Research conducted in the last seven years is mainly focused on theoretical understanding, preliminary selection of materials and experimental verification for PETE.

This review tries to provide an overview on thermionic energy conversion for CSP, including the fundamental principles of solar-induced thermionic emission, the current progress on solar heat-induced thermionic emission (HITE) and photon-enhanced thermionic emission. After a summary of the performance characteristics of TEC hybrid systems, a discussion about practical TEC based CSP and thermodynamics analysis is presented to provide the theoretical guidance for

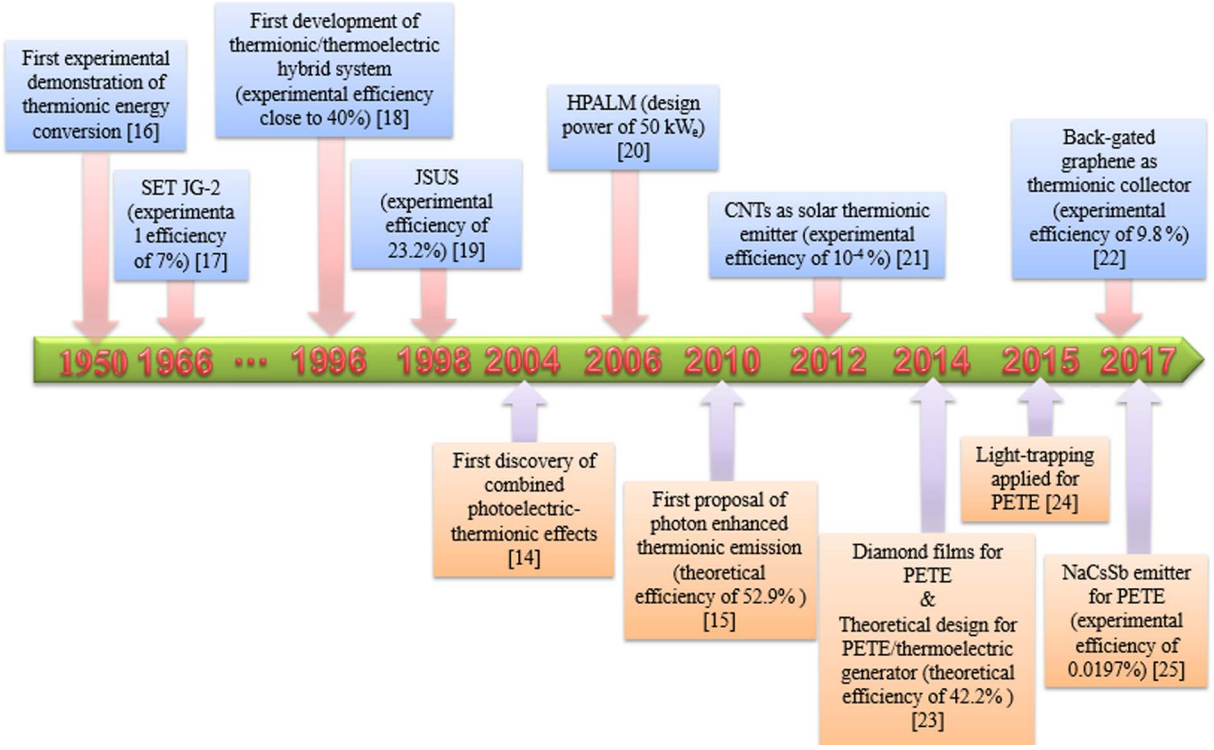

Fig. 1. Overall historical progress on solar thermionic energy conversion.

the combined cycles with conventional heat engines.

2. Basic principles

A typical configuration of concentrating solar thermionic energy converter is shown in Fig. 2, where two electrodes called emitter and collector, respectively, are separated from each other by an intervening space in vacuum and connected to the external load. The emitter that receives light from the solar concentrator can either be a metallic material or a semiconductor, while the collector that disposes waste heat to a heat sink is usually a metallic material. Electrons are thermionically emitted into the vacuum region from the hot emitter when they gain sufficient energy to overcome the potential barrier at the emitter surface; then, they traverse the gap and reach the cold collector. This procedure is generally divided into the electron emission and vacuum transport phenomena, both of which are explained in detail in the following sections.

2.1. Fundamental principle of electron emission

In general, light-harvesting TEC transforms concentrating solar radiation into thermal energy, thereby producing electricity via heat-induced thermionic emission. This process potentially occurs in conjunction with photoemission and photon-enhanced thermionic emission in semiconducting emitters, while only with photoemission in metallic emitters.

2.1.1. Heat-induced thermionic emission

An energy band diagram for heat-induced thermionic emission is shown in Fig. 3(a). A basic solar thermionic emission process is

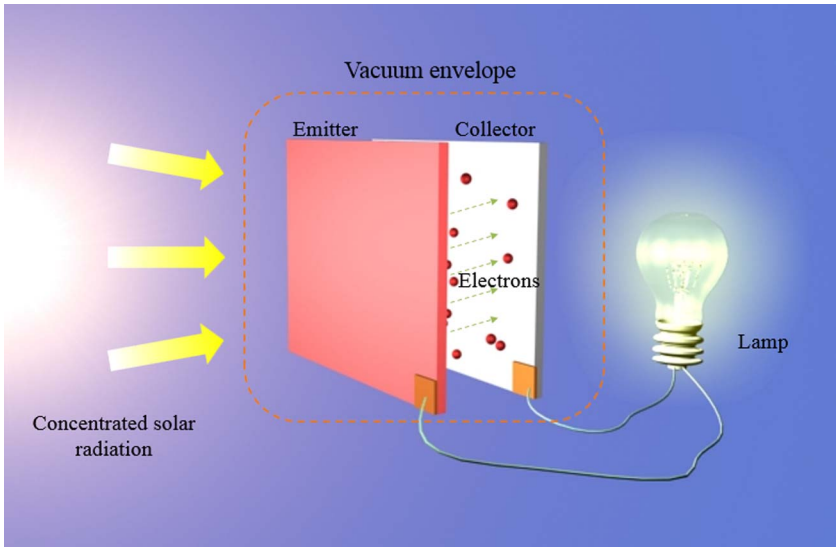

Fig. 2. Typical configuration of the concentrating solar TEC.

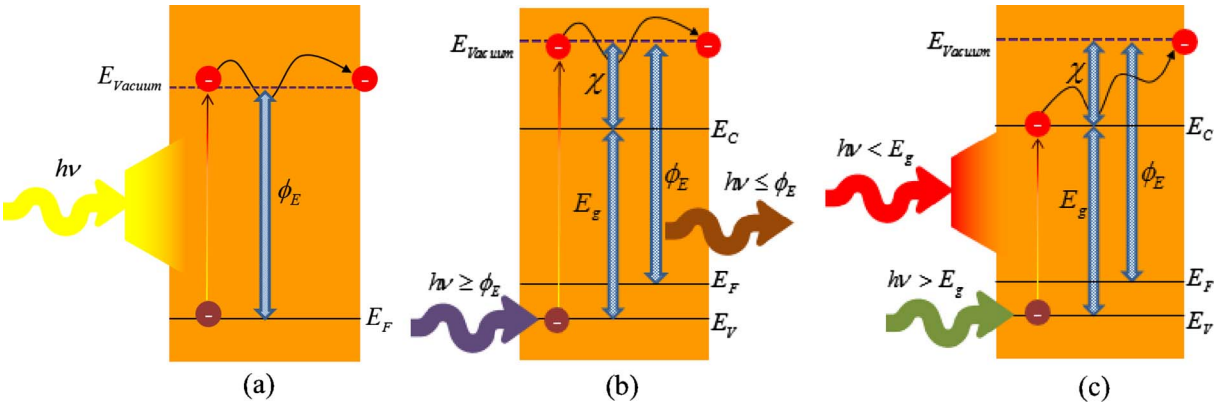

Fig. 3. Energy band diagrams. (a) heat-induced thermionic emission, electrons are initially at E_F in metals but at E_V in semiconductor; (b) photoemission; (c) photon-enhanced thermionic emission.

typically described as follows: solar radiation is converted to thermal energy due to lattice absorption, increasing the energy of electrons in the emitter. If electrons near the surface have higher increased kinetic energy than the emitter work function, they are emitted into vacuum [26].

For heat-induced thermionic emission, all photons are converted to heat. For photoemission, the photons with an energy $h\nu \geqslant \phi_E$ are absorbed to excite electrons to the vacuum level and those with an energy $h\nu < \phi_E$ are transmitted through the emitter. For photon-enhanced thermionic emission, the photons with an energy $h\nu \leqslant E_g$ are converted to heat and those with an energy $h\nu > E_g$ are used to excite electrons from the valence band to the conduction band. $h\nu$ represents the energy of the incident light, E_V and E_C are the valence band maximum and conduction band minimum, respectively, E_F is the Fermi level, and E_g, χ, ϕ_E are the energy bandgap, electron affinity and work function of the material, respectively.

Thermionic electrons emitted from a heated emitter have a half-Maxwellian electron velocity distribution function, which is analytically given as the following [12]:

$$f(v_x) = \left(\frac{2m_e}{\pi k T_E}\right)^{1/2} exp\left(-\frac{m_e v_x^2}{2kT_E}\right) \quad for\ v_x \geqslant 0 \tag{1}$$

where m_e is the mass of the electron, k is the Boltzmann's constant, T_E is the emitter temperature and v_x is the velocity component of the electron in the direction normal to the surface.

The emission current follows the equation [27]:

$$J_{em} = \begin{cases} AT_E^2 exp\left(-\frac{\phi_E}{kT_E}\right) & for\ qV \leqslant \phi_E - \phi_C \\ AT_E^2 exp\left(-\frac{\phi_C + qV}{kT_E}\right) & for\ qV > \phi_E - \phi_C \end{cases} \tag{2}$$

where A is the Richardson constant of the emitter. The theoretical limit value of Richardson constant is 120 A/cm^2 K^2 [28], ϕ_E and ϕ_C are the work functions of the emitter and collector, respectively, q is the electron charge, and V is the output voltage.

In a similar way, the reverse current from the collector electrode has the following relation:

$$J_{rev} = \begin{cases} AT_C^2 exp\left(-\frac{\phi_E - qV}{kT_C}\right) & for\ qV \leqslant \phi_E - \phi_C \\ AT_C^2 exp\left(-\frac{\phi_C}{kT_C}\right) & for\ qV > \phi_E - \phi_C \end{cases} \tag{3}$$

where T_C is the collector temperature. An additional assumption that the emitting electrons are collisionless in the interelectrode gap should be made for this case.

Thus, the ideal power output, which is defined as the electrical power delivered to the electrical load outside the TEC, is given by the relation:

$$P_{TE} = (J_{em} - J_{rev})V \tag{4}$$

The thermionic energy conversion efficiency can be expressed as follows:

$$\eta_{TE} = \frac{P_{TE}}{P_{sun} X} \tag{5}$$

where X is the concentration ratio.

2.1.2. Photoemission

As shown in Fig. 3(b), direct photoemission [29,30] can be decomposed into the following steps based on Spicer's model: electron photoexcitation above the vacuum level, transport of photoelectrons toward the emitting surface accompanied with energy losses due to scattering of phonons or recombination with holes, and emission into vacuum if the kinetic energy is sufficient to overcome the surface barrier.

Photoexcited electrons that do not recombine in the bulk may encounter the emitting surface, where they tend to be reflected, escape into vacuum, or recombine with holes. In addition, the electrons that encounter the back surface will also recombine due to the presence of the substrate [31]. The resulting emission current is written as follows:

$$J_{PE} = \int_0^L \frac{qS_{emission}}{(S_{emission} + S_{recombination})(1 + \zeta exp^{-2d/L}) + D/L(1 - \zeta exp^{-2d/L})} (exp^{-x/L} + \zeta exp^{-(2d-x)/L}) G(l) dl \tag{6}$$

where J_{PE} is the resulting photoemission current density, $S_{emission}$ is the emission velocity, $S_{recombination}$ is the surface recombination velocity, D is the electron diffusion coefficient, $L = \sqrt{D\tau}$ is the electron diffusion length, τ is the bulk recombination lifetime, $\zeta = (D/L - S_{back})/(D/L + S_{back})$ is a dimensionless reduced rate of surface recombination at the back surface, S_{back} is the recombination velocity at the back surface, d is the thickness of the emitter, l is the perpendicular distance from the emissive surface, and $G(l)$ is the rate of photoexcitation of conduction band electrons.

2.1.3. Photon-enhanced thermionic emission

PETE, which harvests both the energy of photons and the thermal energy of solar radiation, favors the energy band diagram illustrated in Fig. 3(c). Here, valence electrons are first excited to the conduction band when the emitter is illuminated with light, and then they rapidly thermalize to the conduction band minimum and diffuse throughout the emitter. Finally, electrons with energies greater than the electron affinity can be emitted into vacuum. PETE exhibits several physical features that differentiate it from photoemission or heat-induced thermionic emission [14]. PETE electrons are thermalized before emission, which results in a thermal distribution of the energies of the emitted electron regardless of the photon energy. In addition, PETE can be

distinguished from HITE by comparing the thermionic current with and without illumination.

Similar to HITE, the ideal PETE current depends on the photoexcited electrons which have sufficient energy to be emitted from the emitter electrode. Consequently, the photon-enhanced thermionic current density can be written as follows:

$$J'_{em} = AT_E^2 exp^{-(\phi_C-(E_{F,n}-E_F))/kT_E} = qn\sqrt{\frac{kT_E}{2\pi m_e^*}}exp^{-\chi/kT_E} \quad (7)$$

where m_e^* is the electron effective mass, $E_{F,n}$ is quasi-Fermi level, and n is the total conduction band population, which is the sum of the equilibrium electron concentration $n_{eq} = 2\left(\frac{2\pi m_n^* kT_E}{h^2}\right)^{3/2} exp\left(-\frac{E_g - E_F}{kT_E}\right)$ and the non-equilibrium concentration dn.

The non-equilibrium concentration can be obtained from the conduction band population equilibrium of the emitter, as follows:

$$\Gamma_{sun} = \Gamma_{PETE} + \Gamma_{recombination} \quad (8)$$

in other words, the photogeneration rate of the conduction band electrons equals to the total rate of recombination and photon-enhanced thermionic emission. In terms of the energy release process, the electron recombination can be categorized as radiative recombination, Auger recombination and Shockley-Read-Hall (SRH) recombination [31,15,32].

The total minority electron lifetime in the bulk can be expressed as follows [33,34]:

$$\tau_n = \frac{1}{B(n + p_{eq}) + (C_n n + C_p p)(n + p_{eq}) + \frac{1}{\tau_{SRH}}} \quad (9)$$

where B is the radiative recombination coefficient, n and p are the densities of electrons and holes, respectively, $p_{eq} = 2\left(\frac{2\pi m_p^* kT_E}{h^2}\right)^{3/2} exp\left(-\frac{E_F}{kT_E}\right)$ is the equilibrium hole concentration, C_n and C_p are the Auger recombination coefficients for electrons and holes, respectively, and τ_{SRH} is the Shockley-Read-Hall (SRH) recombination lifetime, which is directly proportional to the density of the deep-level impurities in the material, and it increases with the injection level.

As in the TEC, the reverse current from the collector is the same as Eq. (3). Therefore, the power output and conversion efficiency of photon-enhanced thermionic emission can be calculated by the following:

$$P_{PETE} = (J'_{em} - J_{rev})V \quad (10)$$

$$\eta_{PETE} = \frac{P_{PETE}}{P_{sun}X} \quad (11)$$

2.2. Fundamental principle of electron transport in vacuum

Electrons emitted into vacuum via either heat-induced thermionic emission, photoemission or photon-enhanced thermionic emission can form a space charge region. The space charge effect hinders the

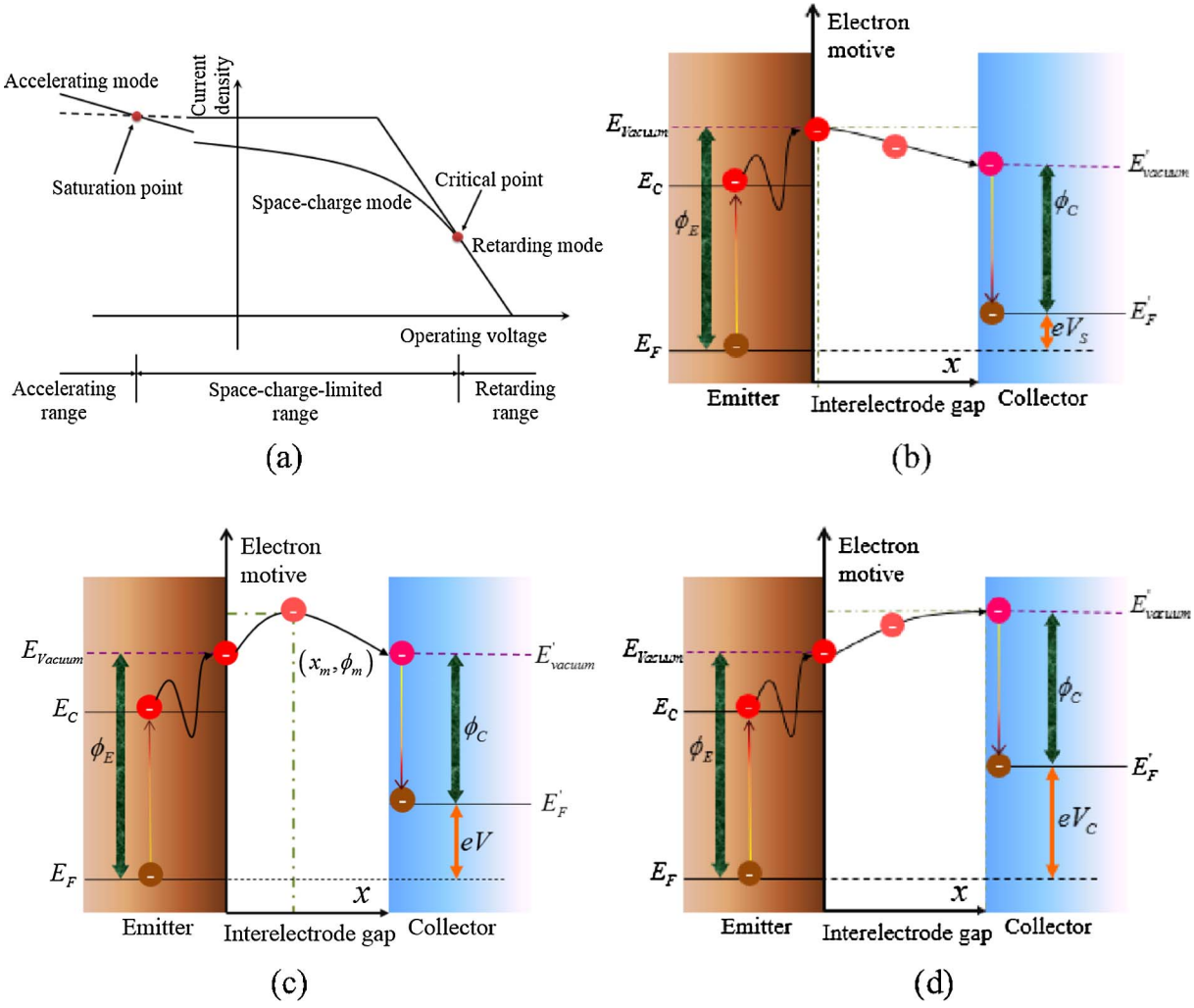

Fig. 4. Typical electron motives for thermionic energy conversion at (a) typical output-current characteristic of a vacuum diode, (b) the saturation point, (c) the space charge limited regime, and (d) the critical point. V_S and V_C represent the voltage output at the saturation point and the critical point, respectively.

electrons to transport to the opposite electrode. A motive diagram $\phi(x)$, showing the potential energy of the electron as a function of x in the interelectrode, is used to conveniently analyze this phenomenon, where x is the distance from the emitting surface. Because the motive is the electrostatic potential multiplied by $-q$, the force on an electron is equal to the negative gradient of the motive [35].

Generally, the interelectrode motive diagram can be divided into the accelerating regime, the space charge-limited regime and the retarding regime, according to the potential distribution, with two junction points referred to as the saturation point between the accelerating and space charge-limited regimes and the critical point between the space charge-limited and retarding regimes, as shown in Fig. 4(a). Fig. 4(b) represents the saturation point, where the maximum motive occurs at a point just outside the emitter. When the output voltage is lower than the voltage of the saturation point, all emitted electrons can be transported through the vacuum space and reach the collector because the forces on the electrons anywhere are directed towards the collector. When the maximum motive ϕ_m is located at x_m in the interelectrode space, as shown in Fig. 4(c), the electrons are constrained by the space charge-limited regime, and they experience a barrier $\phi_m - \phi_E$. Consequently, only a portion of the emitted electrons can finally reach the collector. At the critical point presented in Fig. 4(d), the maximum motive appears just outside the front surface of the collector. If the output voltage is larger than that of critical point, the electrons undergo a decelerating force towards the emitter during their entire travel. Hence, fewer electrons can be gathered by the collector compared to those in the space charge-limited range.

From the quantitative standpoint, the motive diagram $\phi(x)$ in the interelectrode space is governed by the Poisson's equation:

$$\frac{d^2\phi}{dx^2} = -\frac{q^2 N(x)}{\varepsilon_0} \tag{12}$$

where ε_0 is the permittivity of vacuum, and $N(x)$ is the electron number density at position x, which is given by the following:

$$N(x) = \int_{-\infty}^{\infty} dv_y \int_{-\infty}^{\infty} dv_z \int_{-\infty}^{\infty} dv_x f(x,v) \tag{13}$$

where $f(x,v)$ is the distribution function of electrons, and it can be expressed as follows:

$$f(x,v) = 2N(x_m)\left(\frac{m_e}{2\pi k T_E}\right)^{3/2} exp\left(\gamma - \frac{m_e v^2}{2kT_E}\right) \times \begin{cases} \tau(v_x - v_0), x \geqslant x_m \\ \tau(v_x + v_0), x < x_m \end{cases} \tag{14}$$

where $\gamma = \frac{\phi_m - \phi}{kT_E}$, and $\tau(v_x)$ represents a unit step function. In addition, the current density is given by the following:

$$J = 2qN(x_m)\left(\frac{kT_E}{2\pi m_e}\right)^{1/2} \tag{15}$$

As the current–voltage relations are determined by the three cases mentioned above, the power output of the converter can be expressed as follows [35]:

$$P = JV = \begin{cases} qnV\sqrt{\frac{kT_E}{2\pi m_e}}\, exp\left(-\frac{\chi}{kT_C}\right), 0 < V < V_S \\ J\left[(\phi_E - \gamma_{Em} kT_E) - (\phi_C - \gamma_{Cm} kT_E)\right]/q, V_S \leqslant V \leqslant V_C \\ qnV\sqrt{\frac{kT_E}{2\pi m_e}}\, exp\left(-\frac{\chi + (\phi_C + qV - \phi_E)}{kT_E}\right), V_C < V \end{cases} \tag{16}$$

where $\gamma_{Em} = (\phi_m - \phi_E)/kT_E$, and $\gamma_{Cm} = (\phi_m - \phi_C)/kT_E$.

It is worth noting that the Eq. (12)–(16) obtained above are applicable to the condition that electrons undergo collisionless flow in one dimension, and the reverse current is negligible.

3. Heat-Induced solar thermionic conversion

The solar TEC was primarily designed as a competitive candidate as the power source for space probe propulsion. Three renowned solar thermionic conversion prototypes have been established to demonstrate the possibility of operation in space, whose characteristic parameters are listed in Table 1. The Jet Propulsion Laboratory (JPL) [17] developed the first worldwide solar thermionic system by the support of the Solar Energy Thermionics (SET) program in 1961. The optimal thermionic energy converter, which was called JG-2, achieved an electrical power output of 114 W_e and an energy conversion efficiency of 7.0% at an elevated temperature of 1727 °C. After a dormant period of 30 years, the solar thermionic energy conversion resurrects when the Japan Solar Upper Stage (JSUS) program was established in 1998 [19]. This thermionic energy converter delivered a power of 17.9 W and a high conversion efficiency of 23.2% at an emitter temperature of nearly 1577 °C. Subsequently, U. S. Air Force proposed the HPALM solar thermionic system [20], which achieved a maximum power of 30 W_e at an emitter temperature of 1397 °C.

The power output and conversion efficiency rely on the overall system configuration and specific material properties of the TEC [36]. Olukunle et al. [37] discussed the dependence of the conversion efficiency on system parameters, such as the height and radius of the concentrator aperture and found that energy losses due to system configuration can be easily reduced. However, the energy conversion efficiency is significantly limited by the intrinsic properties of TECs, i.e., non-ideal electron emission, space charge effect in the vacuum space and collection nature [38]. Table 2 shows some experimental results about practical TECs. The primary methods for improving thermionic energy conversion efficiency is listed in Table 3.

3.1. Enhancing thermionic emission

As in the cases of TEC prototypes mentioned above, because of the extremely high operation temperature, refractory metals with relatively low vapor pressures are preferred as electrodes, such as tungsten (4.54 eV), rhenium (4.7 eV), molybdenum (4.15 eV), etc (shown in Table 4). Nevertheless, their relatively high work function prevents the thermionic emission from achieving an optimum ideal performance. Therefore, lowering the emission barrier of the emitter at all costs could be an effective way to improve the electron emission and thus the power output of TEC. Although the electron emission dramatically

Table 1
Characteristic parameters for several designed solar TECs.

Project	System configuration	Emitter and collector materials	Emitter temperature (°C)	Electrical power output (W)	Conversion efficiency
SET [17]	3 m diameter parabolic rigid mirror coupled with 5 TECs	Emitter: Re Collector: Mo	1727	114	7.0%
JSUS [19]	1.6 m diameter paraboloidal concentrator accompanied with planar single crystal Mo converter	Single crystal Mo	1577	17.9	23.2%
HPALM [20]	6 m diameter concentrator mirror with cylindrical inverted converter	Emitter: tungsten single-crystal Collector: Mo-3% Nb single crystal	1397	30	–

Table 2
The experimental results about practical TECs.

Author (year)	Emitter material	Collector matrial	Emitter temperature (°C)	Collector temperature (°C)	Voltage Barrier (V)	Interelectrode gap (mm)	Cesium temperature/ vapor pressure	Power output (W/cm2)	Efficiency
Rufeh (1972) [39]	Tungsten oxide	Polycrystalline tungsten	1527	600		0.5	294 °C	6	
Hansen (1976) [40]	Tungsten	Nickel	1147	577		2.5	293 Pa (Argon)	1	
Shimada (1977) [41]	Grooved molybdenum	Molybdenum	1227	455	1.96	1.7	220 °C	0.95	
Henne (1980) [42]	ZrO2-Mo	ZrO3-Mo	1250		1.95	0.5	220 °C	2.5	
Goodale (1980) [43]	SiC-C-W	Nickel	1357	627	2.1	0.2	280 °C	2.1	
Smith (1980) [44]	Molybdenum	Stainless steel	1327	677	192	0.5	266 Pa	6	
Stark (1980) [45]	Molybdenum	Molybdenum	1377	477	2.32	0.25		4	
Goodale (1982) [46]	SiC-C-W	Nickel	1102	627	2.2	0.2		0.2	0.50%
Dick (1983) [47]	Tungsten	Nickel	1180	318	1.74	0.0119		4.2	
El-Genk (1999)	Molybdenum	Molybdenum	1300	800		1.5	150 Pa	0.34	4.90%
El-Genk (2002) [48]	Molybdenum	Molybdenum	1400	700	1.88	0.5	140 Pa	2.27	15.10%
	Tungsten	Niobium	1327	727		0.5	245 Pa	1.76	7.90%
Momozaki (2004) (macro-grooves 0.5 mm wide, 0.5 mm deep and 1.0 mm apart) [49]	Grooved molybdenum	Smooth molybdenum	1400	600	2.1	0.5	241 Pa	2.18	12.90%
	Smooth molybdenum	Grooved molybdenum	1400	600	1.86	0.5	241 Pa	2.56	14.70%
	Smooth molybdenum	Smooth molybdenum	1400	600	1.92	0.5	241 Pa	3.74	17%
	Grooved molybdenum	Grooved molybdenum	1400	600	2.06	0.5	241 Pa	1.86	11.20%

Voltage barrier = collector work function + arc drop voltage + attenuation voltage.

increases when the emitter barrier is lowered, the power output does not necessarily increase. One reason for this is that a higher emitter current output results in a larger space charge effect. Lowering the emitter barrier is only beneficial to a relatively small extent due to the self-limiting nature of the space charge effect. The second reason is that the power output depends on the product of a current output and an output voltage. Lowering the emitter's work function by depositing materials with low work function, e.g., cesium (2.14 eV) or barium (2.7 eV), on the substrate is a common solution. Koeck et al. [50] explored the effects of molybdenum, tungsten and rhenium substrates on the electron emission properties and concluded that the work functions of these emitters are similar while the thermionic current differ markedly when exposed to Cs vapor. Another interesting method of reducing work function is by micro/nanostructure geometry engineering of the emitter surface [51]. Barabash et al. [52] stated that the thermionic current from emitter of developed surface is 3–4 times higher than that from smooth surface emitter, which can be explained by the increased surface area and plasma penetration. These factors can lead to a reduced effective work function of emitter, which is consistent with the research conducted by Busygin et al. [53]. The micro-scale ridge arrangement may lead to significant angular variations in the macroscopic current density [54], which facilitates electron transport toward the collector and thus increases the overall thermionic current. Zeng proposed a multilayer nanostructured vacuum TEC by using the quantum tunneling effect [55]. It is stated that a series of quantum wells are formed on the surface and electrons are hampered from filling the energy levels, which raises the chemical potential and thus reduces the work function.

Although refractory metals are ideal materials from the viewpoint of their high material strength, chemical inertness and high thermal/electrical conductivity, their thermionic performance suffers severely due to the intergranular embrittlement at elevated temperatures, which drives research via the top-down approach into the field of nanotechnology. The nanomaterials have the potential to surmount the challenges of conventional TECs due to the superior thermal and optical characteristics [67]. Liang et al. studied the thermionic emission of graphene and proposed a graphene-based thermionic energy converter, which can exhibit a high theoretical conversion efficiency of up to 45% [68]. Other nanomaterial-based emitters, such as nanostructured carbon materials, sulfur-doped nanocrystalline diamond [69] and carbon nanotubes (CNTs), have been extensively studied for HITE. The electron emission barriers of these materials are lowered by a non-uniform spatial distribution of the field enhancement [70].

Diamond, in conjunction with suitable donors, has exhibited potential for thermionic energy conversion mostly due to its considerably lower operating temperature of less than 1000 °C and lower effective work function of less than 2 eV [64]. The most attractive diamond is the nitrogen-doped diamond, which contains a surface with a negative

Table 3
Methods for improving thermionic energy conversion.

Targets	Emitter: enhancing thermionic emission	Interelectrode gap: reducing space charge effect	Collector: optimization of collector
Detailed methods	Depositing low work function materials	Inserting cesium vapor into the interelectrode gap	Lowering work function
	Micro/nanostructure geometry engineering of the emitter surface	Employing negative electro affinity electrode	Surface morphology
	Exploiting nanomaterial-based emitters such as graphene, carbon nanotube films and doped diamond films	Electrostatic triode configuration	Selection of operation temperature with different thermionic converters
		Molecular assisted charge transport	
Comments	These optimization methods lower the emitter work function and increase Richardson constant, related to Eq. (2)	These optimization methods help transport emitted electrons to collector with minimal barrier in interelectrode, related to Eq. (16)	These optimization methods increase output voltage and decrease reversed (and reflected) electrons, related to Eq. (3)

Table 4
Feature parameters of thermionic emitter material.

Emitter material	Work function (eV)	Richardson constant (A/cm^2 K^2)	Emitter material	Work function (eV)	Richardson constant (A/cm^2 K^2)
Limiting value	0.9 (the lowest work function achieved)	120			
Tungsten [56]	4.54	55–104	Diamond on Rhenium [50]	1.34	53.1
Molybdenum [57]	4.15	39	Nanocrystalline diamond [62]	1.29	0.84
Rhenium [58]	4.7	110	Nitrogen-incorporated polycrystalline diamond on Mo [63]	2.22	5.96
Cesium on Tungsten [12]	1.36	3.2	Nitrogen-doped nanocrystalline diamond [64]	1.99	70
BaO [59]	1.5	0.1	Nitrogen-doped diamond with NEA [65]	1.5–1.9	0.1–10
Carbon nanotubes [60,61]	2	110–120	Heavily phosphorus-doped diamond [66]	2.3	15

electron affinity after hydrogen treatment and N impurities as the electron donors. Koeck et al. developed nitrogen-doped nanocrystalline diamond films with a low effective work function of 1.99 eV and a high Richardson constant of ~70 A/cm^2 K^2 [65]. However, the upward band bending due to the surface roughness and inhomogeneity of the polycrystalline film inhibits thermionic electron emission. One possible solution may be homoepitaxial growth, which reduces the upward band bending from ~1.7 eV to 0.7 eV [71]. Another advanced emitter material is phosphorus-doped diamond, where shallow donor states along with a narrowed space charge width can lower the barrier for HITE. The effective work function can reach to a value of 0.9 eV, while the Richardson constant reduced to a poor value of 10 μA/cm^2 K^2 [72]. Heavy doping using phosphorus with a concentration of over 10^{20} cm^{-3} can significantly elevate the Richardson constant to 15 A/cm^2 K^2 [66].

Loutfy et al. [73] compared the performance of CNTs with those of tungsten and hydrogenated nitrogen-doped diamond and concluded that CNTs exhibit a better thermionic emission due to the superior temperature stability. Meanwhile, it is reported that the work function of CNTs is effectively decreased to approximately 2.0 eV at 327 °C with the intercalation treatment of alkali metals [60]. Additionally, the CNTs have the ability to overcome the dissipation of heat. When an array of multiwalled CNTs is illuminated by a concentrated light, a heat-trap effect occurs, as shown in Fig. 5. Meanwhile, the energy loss due to incandescence from the hot spot can be substantially reduced by reducing the work function of the CNTs. It is calculated that CNTs have a faster increase of temperature (~2000 K at 100 W/cm^2 solar radiation) and higher efficiency (~50% at 1000 W/cm^2 solar radiation) due to heat trap effect as compared to isotropic bulk materials [21,74,75]. It was discovered [76] that electrons run away from the lateral surface of CNTs because the hot forward-scattering optical phonons facilitate electron emission.

3.2. Reducing space charge effect

Scientists reported that the optimal interelectrode gaps in conventional TECs is in the range of 0.9–3 μm, which is approximately equal to the characteristic wavelength of the thermal radiation of the emitter [77]. The practical fabrication of an emitter–collector assembly which

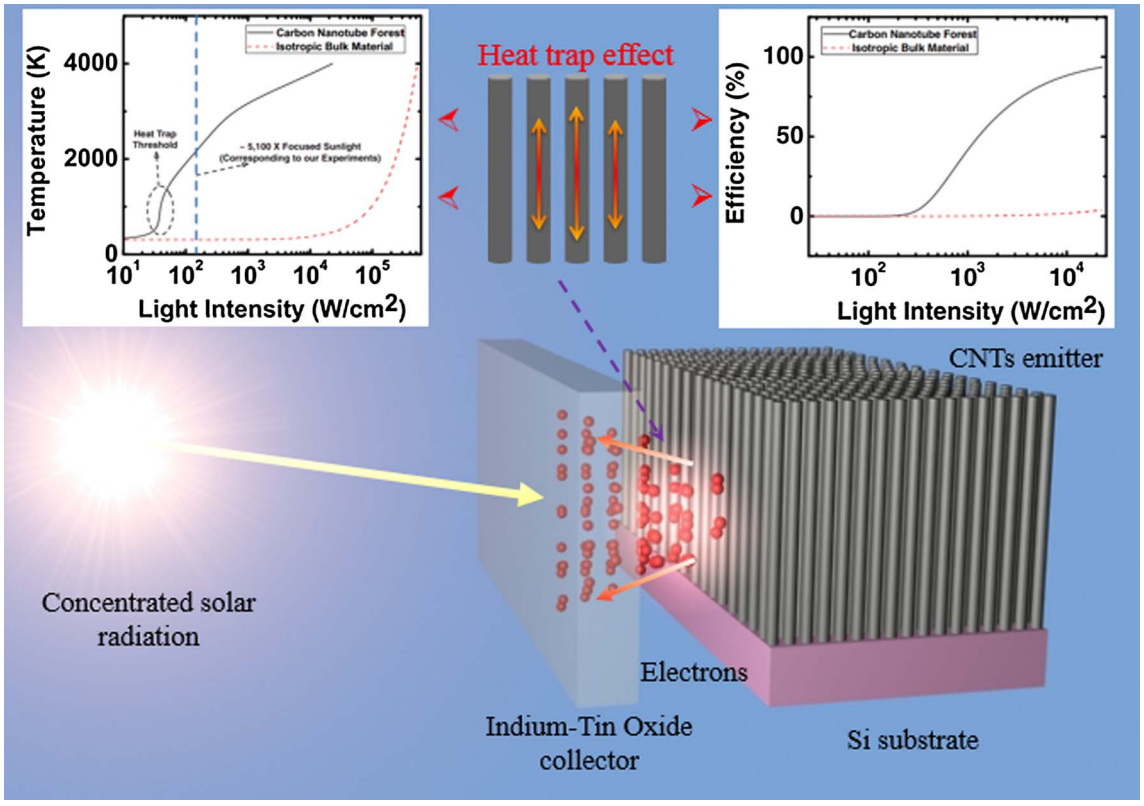

Fig. 5. CNTs-based solar TEC. Heat trap effect occurs in CNTs due to the intrinsic property of quasi-one-dimensional heat-transfer nature.

operates at a large temperature difference of hundreds of Celsius within a required close tolerance is highly challenging. High-temperature operation in TECs with such interelectrode gaps is also difficult because they may risk short circuit of the device due to thermal expansion of the electrodes. For gaps < 0.9 μm, the near-field evanescent-wave radiative heat transfer, which is sometimes referred to as tunneling of evanescent waves [78], can be increased by many orders of magnitude, resulting in a reduction of the conversion efficiency. Conversely, for gaps > 3 μm, space charge clouds dominate the transport of electrons and decrease the overall outputs [79]. Fortunately, the space charge effect can be mitigated and converted to power output by altering the electric potential distribution in the interelectrode gap [10]. A number of methods have been successively introduced to reduce space charge effect, as shown in Fig. 6, including the insertion of Cs ions into the interelectrode region, the use of a negative electron affinity (NEA) emitter, the electrostatic triode configuration and the exploitation of molecular assisted charge transport.

The most successful and widely used method to overcome space charge effect is by filling the interelectrode gap with cesium. Lee et al. reported that the performance of microfabricated SiC TECs are enhanced by ~1.5 times with cesium coating [80]. Three beneficial phenomena occur when cesium vapor is introduced. First, the cesium adsorbed on the surfaces of the electrodes can reduce work functions, which induces more electrons to emit into vacuum. Second, the adsorbed cesium atoms are thermionically emitted from the surfaces of the electrodes as cesium ions, and they neutralize the emitted electrons to mitigate the space charge effect. Finally, the cesium vapors in the interelectrode gap can in turn be ionized due to collision with emitted electrons, further reducing the space charge effect. Based on the mechanism of electron production, cesium TECs can be divided into two groups, i.e., the ignited and unignited modes [81]. The significant difference between these two modes is how to maintain a neutral plasma. The plasma can be generated by collision process between electrons and Cs vapors in the ignited mode, while produced by thermionic emission of Cs ions in the unignited mode. For energy conversion applications, the ignited mode in the TEC is preferred because of its higher electrical power output, whereas conversion efficiency is comparable to the unignited mode.

The second method to reduce the space charge effect is to use a negative electron affinity material as the emitter electrode. One common technique to obtain a NEA material is the synergistic treatment of cesium and oxygen on the surface of emitter electrode. Another method is hydrogen plasma treatment on doped diamond film, which can form a dipole surface due to ionic C—H bond. TECs with NEA emitters have a lower emitter temperature and intrinsic reduced space charge effect because the NEA property lowers the electrostatic boundary condition just outside the emitter electrode. In other words, the electrons emitted from NEA surface have a greater kinetic energy as

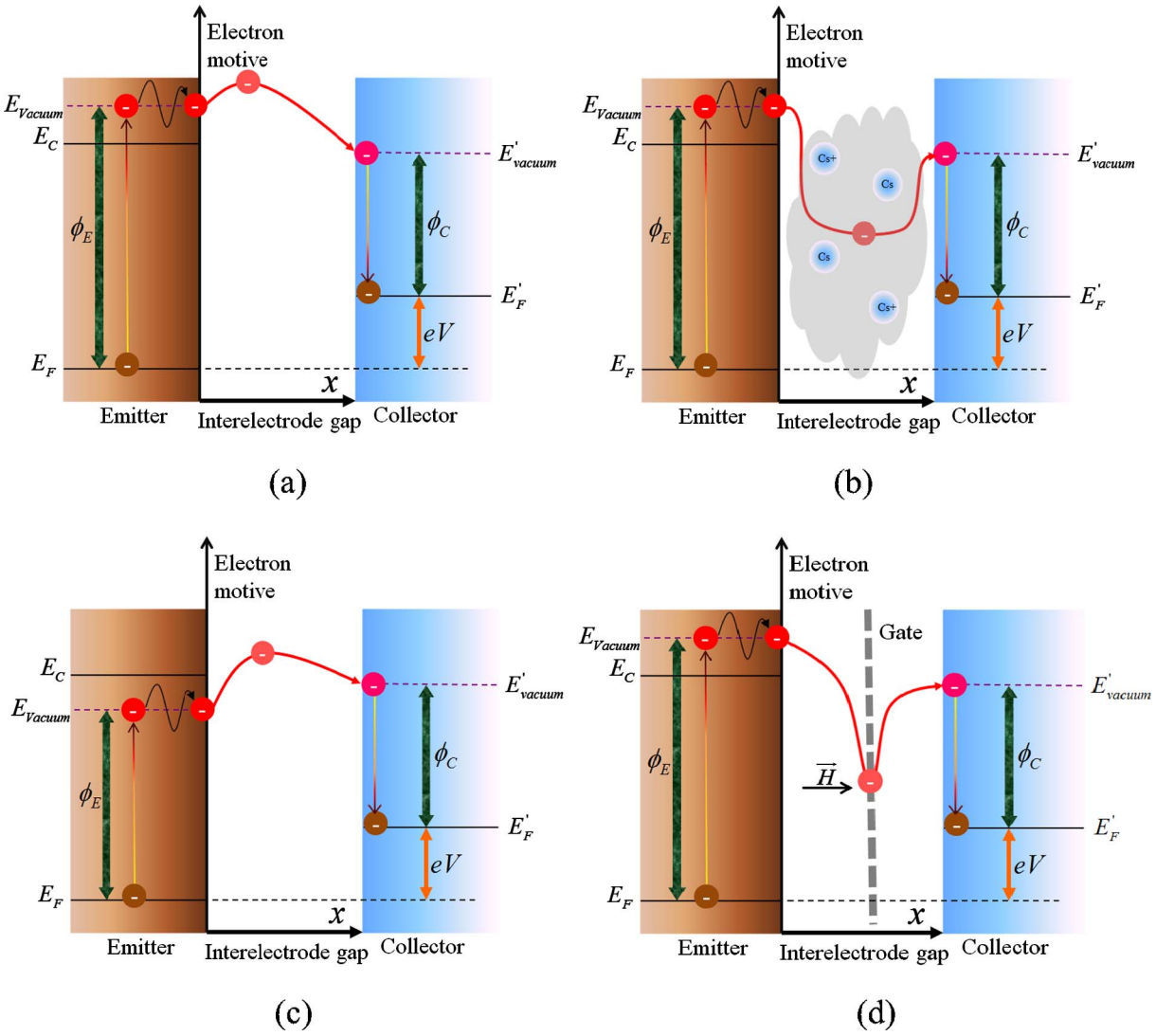

Fig. 6. Interelectrode motive of (a) original TEC, (b) TEC with cesium filling, (c) TEC with negative electron affinity emitter, and (d) magnetic triode TEC.

compared to those from PEA surface [82,83].

The third method is to use a positively charged gate electrode that is placed between the emitter and collector electrode. The charged gate electrode can create a potential trough to reduce the static space charge effect. This trough can accelerate the emitting electrons away from the emitter surface and decelerate them as they approach the collector. Mannhart's group suggested that graphene or related 2D materials can be treated as gate electrode due to the high transparency of ~60% for electrons with energies between 2 and 40 eV [84,85]. Another independent group of Srisonphan reported that ~99.9% of electrons, whose energy is < 3 eV, can be transported through a graphene film, indicating an excellent potential for gate electrode. An additional homogeneous magnetic field is usually applied to direct the electrons through the grid-holes of the gate electrode. It was observed that the current output with 200 mT magnetic filed is 4 times higher than that without magnetic field. One can suggest that by optimizing the gate geometry, the space charge effect can be reduced to a large extent [10].

Recently, a new concept of incorporating molecular assisted charge transport in the interelectrode gap was proposed [86]. This innovative method employs the suitable gaseous species (such as methane for diamond emitter) as the electron transport molecule. The reasons for mitigating space charge effect can be explained in two ways. First, the molecular gases gain electrons as they collide with the emitter surface and transport it to the collector electrode. Second, when the emitter's temperature is elevated, surface ionization happens and negative ions are produced. Additionally, the generated positive ions facilitate the recovery of surface state (such as reactivation of diamond film from hydrogen degradation). In essence, molecular assisted charge transport, which shows a promising performance, plays a similar role as cesium filling in the interelectrode gap. It is reported that output power was enhanced by ~2 times within methane at 3 Pa.

3.3. Modification of the collector

The properties of the collector electrode, such as the work function, surface morphology, and operating temperature, have a great effect on the electrical output and conversion efficiency. However, little attention has been paid to the optimization of the collector [38,87].

Typically, the collector work function should be lower than the emitter barrier. A theoretical efficiency of ≥20% was reported for a TEC with a negative electron affinity collector. Some refractory metal oxides, such as WO_x, MoO_x, and AgO_x, have been employed as a low work function collector and studied for an oxygenated TEC [88]. The collector electrodes were fabricated by depositing metal oxide materials on metal substrates in an Ar/O_2 gas mixture. Hence, a TEC with a plane-parallel geometry of a polycrystalline W emitter and the metal oxide collectors (AgO_X, NbO_X and PtO_X) was set up. For the W-AgO_X based TEC, the collector work function was 1.35 eV. Similarly, work functions of 1.38 eV and 1.40 eV were obtained for the W-NbO_X and W-PtO_X converters, respectively. Yuan et al. reported a novel TEC prototype that using back-gated graphene as the anode. It is demonstrated that electrostatic gating of graphene reduces the graphene work function from 1.85 to 1.69 eV, leading to a relatively high TEC efficiency (9.8%) [22].

The surface morphology of the collector electrode can significantly affect the performance of TECs. The converter with grooved collector has a better thermionic performance than that with smooth collector, which is attributed to the increased surface area and correspondingly enhanced plasma density [89]. The non-ideal electrode surfaces, e.g. impurities, vacancies, dislocations and imperfect grain boundaries [12], can result in electron scattering and back reflection, are detrimental to the thermionic performance [90]. It is stated that the structure and chemical composition of the surface can affect the electron reflection. Trapping incident electrons within multiple reflection structure can mitigate the degree of electron reflection. Additionally, the thermionic performance can be enhanced if the collector is covered with matte black materials, such as platinum black, voided nickel and etched electroless Ni-P.

The temperature of the collector also affects the performance of TECs, and the influence varies for different thermionic converter configurations. Momozaki et al. [49] explored the dependence of the temperature on the performances of four different converters, i.e., a smooth-smooth electrode pair, a smooth-grooved electrode pair and a grooved-smooth electrode pair, a grooved-grooved electrode pair. Their results showed that the grooved-grooved electrode converter exhibited the best performance at a temperature of collector of > 973 K, while the smooth-smooth electrode converter exhibited the best performance when operated at an optimum temperature of collector, i.e., ~800 K. The grooved collector TEC can achieve a best overall efficiency of ~35%, when a bottoming cycle of potassium alkali metal thermal to electric conversion is employed.

4. Photon-enhanced solar thermionic conversion

As discussed in the previous section, heat-induced thermionic energy converters require heating of the emitter up to nearly 1400 °C, which is challenging even with the most advanced solar concentrators. To decrease the operation temperature but retain the performance, scientists have explored alternative methods for heat-induced thermionic conversion. Smestad [14] first discovered a synergy mechanism of thermionic emission and photoemission, where combined heating and illumination on a commercial photodiode produced a higher electrical power output than the individual power output of either heating or illumination alone. Subsequently, in 2010, Schwede et al. [15] first proposed a mechanism of PETE that can be applied for solar energy conversion, which integrates the photovoltaic and thermionic effects

Table 5
Progress on the numerical simulation of the optimal efficiency with key parameters for photon-enhanced TECs.

Author (year)	Modified contents	E_g (eV)	χ (eV)	ϕ (eV)	T_E (°C)	T_C (°C)	C	Gap width	η_{PETE}
Schwede (2010) [15]	Original numerical simulation of PETE	1.4	1.0	0.9	1000	227	1000	–	43.0%
Varpula (2012) [33]	Considering diffusion and recombination of photoelectrons	0.95	0.4	0.9	527	300	1000	–	15.0%
Segev (2012) [97]	Considering return electrons contribution to outputs	1.4	0.4	0.9	1136	227	1000	–	44.7%
Segev (2013) [32]	Considering recombination and electron concentration change	0.95(Si)	0.1	0.5	557	227	1000	–	31.3%
		1.03	0.1	0.5	809	227	1000	–	31.4%
Su (2013) [98]	Considering thermal radiation and heat losses	1.36	1.01	0.9	897	245	1000	–	37.9%
Su (2014) [35]	Considering space charge effect	1.42	0.9	0.9	727	227	1000	2 μm	24.2%
Segev (2015) [99]	Considering space charge effect and return electrons contribution to outputs	1.4	0.4	0.9	997	227	628	3 μm	38.0%
Varpula (2015) [95]	Comparisons of Si, GaAs and InP emitters for PETE	1(Si)	0.4	0.9	427	300	1000	–	11.2%
		1.23(GaAs)	0.4	0.9	427	300	1000	–	20.0%
		1.21(InP)	0.4	0.9	427	300	1000	–	23.4%
Wang (2016) [100]	Exploring nanoscale vacuum gap for PETE	1.4	0.5	0.9	1048	227	1000	40 nm	48.6%

E_g and χ represent the bandgap and electron affinity of the emitter, respectively, ϕ is the work function of the collector, T_E and T_C are the temperatures of the emitter and collector, respectively, C represents the concentration ratio, and η_{PETE} is the conversion efficiency of PETE alone.

into a single physical process. The photon-enhanced TEC has a similar parallel-plate structure as the heat-induced TEC, except for a semiconductor as the emitter [91,92]. The semiconductor emitter can exploit both the quantum energy of photons and the thermal energy of solar radiation. By absorbing photons within energies larger than the bandgap of the emitter, valence electrons are promoted into the conduction band. After excitation, electrons rapidly thermalize within the conduction band and diffuse throughout the cathode: electrons that encounter the surface with energies greater than χ can emit directly into vacuum and reach the collector. Recent years have seen a rapid development of PETE, which can be generally divided into three categories, i.e. positive electron affinity (PEA) emitter based PETE conversion, negative electron affinity emitter based PETE conversion and all-solid-state PETE conversion (i.e. avoiding the vacuum gap between emitter and collector).

4.1. Positive electron affinity emitter based PETE conversion

The photocathode with positive electron affinity is widely used as the emitter for PETE, both experimentally and theoretically. Wang et al. [25] employed NaCsSb photocathode as an emitter of PETE. It is obtained that the energy conversion efficiency is 0.0197% under 400 nm illumination at 20 °C and doubles when the temperature rises to 70 °C. There are a majority of theoretical advances made for the optimal conversion efficiency of PETE over the last six years, as shown in Table 5. It is obtained that the optimal bandgap of the emitter is between 1.1 and 1.7 eV, with a finite optimum value of 1.35 eV [15]. A relatively high bandgap, on one hand, will obstruct the use of the quantum energy of the solar source. For example, only 1% of solar photons have energies that exceed the bandgap of GaN (3.42 eV @ 300 K), thus resulting in a very low quantum efficiency, on the order of $\sim 10^{-4}$–10^{-3} electrons per incident photon and consequently making it unsuitable for photon-enhanced thermionic conversion. Additionally, a higher bandgap leads to a larger electron affinity, which requires a higher temperature to produce an identical current and entails a more effective cesium treatment. However, the frequently used Cs-based coatings are unstable at higher temperatures [93,94]. On the other hand, a relatively low bandgap will drastically increase the thermionic cooling and consequently lower the operating temperature of the emitter, which weakens the performance of PETE. When the bandgap of emitter decreases, less photon energy is used for heating the emitter. Moreover, more photoelectrons are generated for thermionic emission and their carried kinetic energy decrease the emitter's temperature. Overall, the performance of PETE converter will decline. Varpula et al. [95] theoretically compared the use of Si (1.12 eV @300 K), GaAs (1.42 eV @300 K), and InP (1.34 eV @300 K) as emitter. They concluded that the larger bandgaps of GaAs and InP lead to higher flat band voltages and higher efficiency as compared to Si for an identical electron affinity (20–25% for GaAs and InP versus 10–15% for Si). Reck et al. [96] presented experimental results on PETE in highly doped cesiated n-type and p-type silicon. The work function of silicon can be lowered from 4.5 eV to 2.1 eV by cesium coating of the silicon surface, and the stability can be maintained over time with an operating temperature of up to 277 °C. The photon enhancement due to illumination is found to be larger in p-type silicon, as predicted by theoretical models. The increase in thermionic current is 1.6 times that of n-type silicon. The reason is that n-type silicon has a smaller difference between the electron quasi Fermi level and the Fermi level as compared to p-type silicon, resulting in lower enhanced electron population in conduction band.

A GaAs emitter with cesium deposited on the p-GaAs (0 0 1) surface seems to be a suitable option for several reasons [30]. First, the bandgap of GaAs is close to the optimal value. Second, the surface potential barrier can be adjusted to an optimum level by cesium deposition, which reduces the electron affinity from ~3.5 eV at the clean GaAs surface to ~0.1–0.2 eV with Cs coverage. Finally, GaAs exhibits a

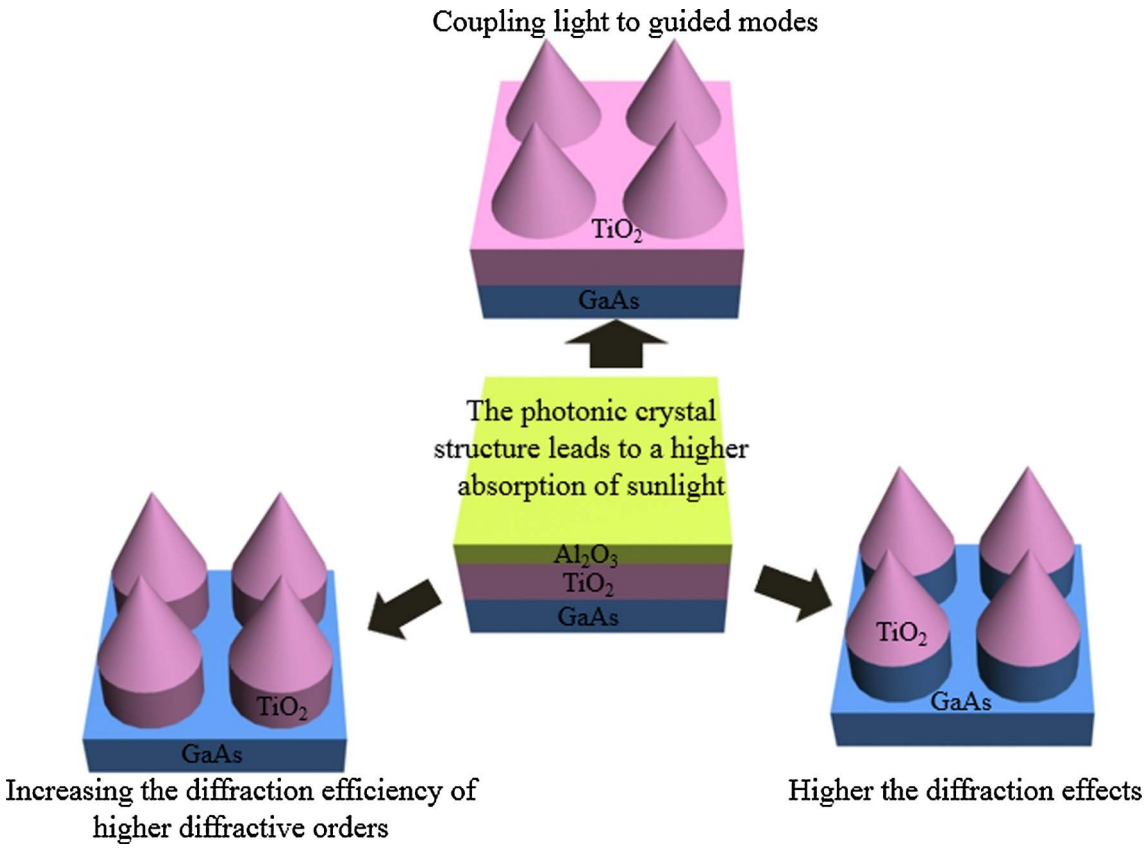

Fig. 7. Photonic crystal structures for light trapping.

high electron mobility of up to 8000 $cm^2/V{\cdot}S$. The absorption characteristics of the GaAs emitter can be further optimized via the construction of a series of photonic crystal structures, as observed in Fig. 7. This light-trapping structure can reduce the bulk recombination and increase the performance by 2% over an optimal bilayer anti-reflective coating [24]. Another potential method of enhancing light absorption is plasmonic nanostructure [101,102,103]. Though the GaAs/Cs emitter exhibits the excellent features described above, the potential use of this configuration in photon-enhanced solar thermionic converters is complicated. The reasons may include the thermal instability of Cs overlayers, the electron scattering at the semiconductor-vacuum interface and a low conversion probability of a Bloch electron in the crystal into a free electron in vacuum [29,104].

The electrical contact configuration, i.e. front contact or back contact, has a significant impact on the performance of photon-enhanced TECs. Generally, the back contact configuration is superior over a front contact configuration, which is mostly due to reduced Ohmic losses and the effective capture of IR radiation [105]. During PETE conversion, photoelectron generation always competes with electron recombination, which is harmful to the thermionic emission yield [31]. The critical recombination mechanism is surface recombination for PETE. The back surface recombination significantly decreases the performance due to an intrinsically high recombination velocity at the metal–semiconductor contact. The effective surface recombination velocity of the majority carriers at the contact is usually assigned a very high value (10^7 cm/s), while that of the minority carriers can vary between 10^2 cm/s and 10^6 cm/s, depending on the type of substrate [106]. It has been stated that the surface recombination will have a weaker effect on the transit process under high injection of electrons, which would enhance the conversion efficiency [34]. An efficient GaAs/$Al_{0.15}Ga_{0.85}As$ heterostructure that introduces an internal interface was proposed by Schwede et al. In this PETE process, shown in Fig. 8, a fraction of the electrons that absorb photons with energies larger than $E_{g,GaAs}$ will jump to the conduction band, and then they are thermalized to the lattice temperature, while other photoexcited electrons that absorb energies larger than $E_{g,GaAs} + \Delta E$ can transit into the emitter layer due to internal photoemission. Moreover, the electrons in the emitter can emitter via direct photoemission when they absorb photons with energies larger than $E_{g,Al_{0.15}Ga_{0.85}As}$. It is reported that this special configuration causes a dramatic improvement in the conversion efficiency because of the reduced back surface recombination [107].

On the other hand, Sun's group [108,109] developed an GaAs heterostructure emitter with a graded bandgap of $Al_xGa_{1-x}As$ (window layer), as observed in Fig. 9. The bandgap gradation of the window layer causes a built-in electric field, which can reduce the contact surface recombination and impel the photo-excited electrons into the emitter, ultimately improving the conversion efficiency. This field is independent of temperature, resulting in a stable efficiency enhancement at high temperatures. It is reported that the efficiency of the $Al_xGa_{1-x}As$/GaAs emitter is 2.6 times that of a GaAs emitter under 1000 concentration ratio.

Similar to heat-induced TECs, electrons in the vacuum gap of photon-enhanced TECs form space charge clouds and inhibit the emission of subsequent electrons, which causes a reduction in the conversion efficiency. Fortunately, these electrons, along with those emitted from the collector, can be first absorbed by the emitter to occupy the conduction band and then can be reemitted into vacuum. This form of electron recycling makes photon-enhanced TECs less susceptible to space charge loss [109]. When a nanoscale gap is considered, the resulting electron tunneling and image force effect are substantial, and the barrier of the emitter can be reduced, which has been discussed for thermionic energy converters [100,110]. However, it is not feasible from a practical point of view mostly due to the high-precision packaging technology. When the gap width between two electrodes is a few microns or more, the space charge effects become important for the photon-enhanced solar TEC. At these distances, the near-field heat transfer effects are negligible because the gaps are larger than the characteristic wavelength of the thermal radiation, as demonstrated by Wien's displacement law. The space charge effects become more obvious as the gap width increases further. In contrast, when the gap width decreases, the space charge effects will be weakened, and thus the device performance will be improved [17].

As confirmed previously, cesium treatment is an ideal and practical solution for improving the performance of a TEC, not only for reducing the work function but also for mitigating space charge effect. Unlike heat-induced TECs, the typical contact ionization of cesium deposited on the emitter alone will not be enough to maintain a sufficiently high plasma density in the interelectrode gap at lower emitter temperatures (< 830 °C). However, it is shown that photoexcitation can reduce the effective ionization potential of cesium, resulting in a sufficient cesium ionization to maintain a neutralizing plasma at relatively low emitter temperature. Indeed, Cs, Cs^*, and $Cs+$ particles collide with the emitter

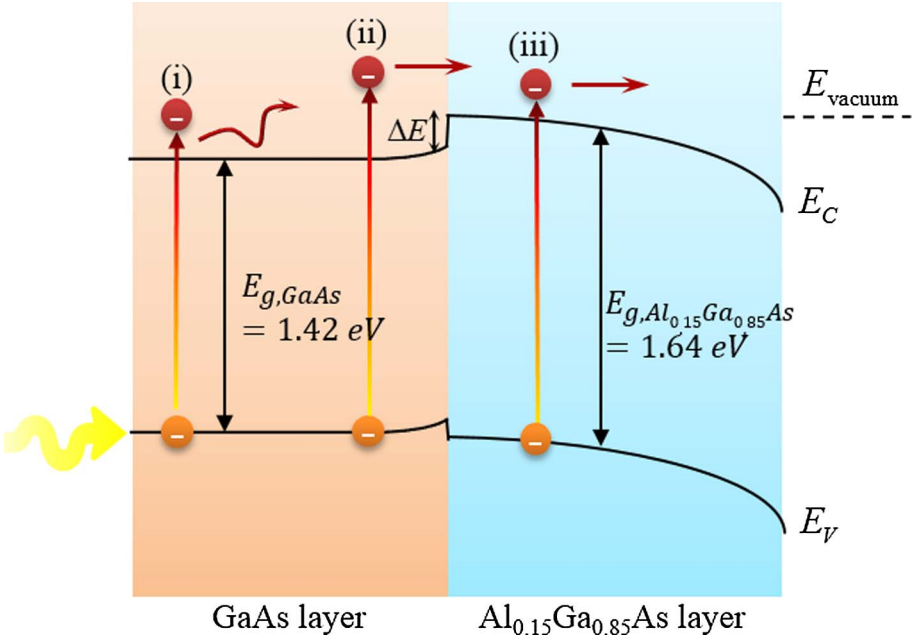

Fig. 8. Schematic band diagram of GaAs/$Al_{0.15}Ga_{0.85}As$ heterostructure. (i) PETE in GaAs layer; (ii) internal photoemission in the absorber and the generated electrons transport into $Al_{0.15}Ga_{0.85}As$ layer; (iii) direct photoemission in $Al_{0.15}Ga_{0.85}As$ layer.

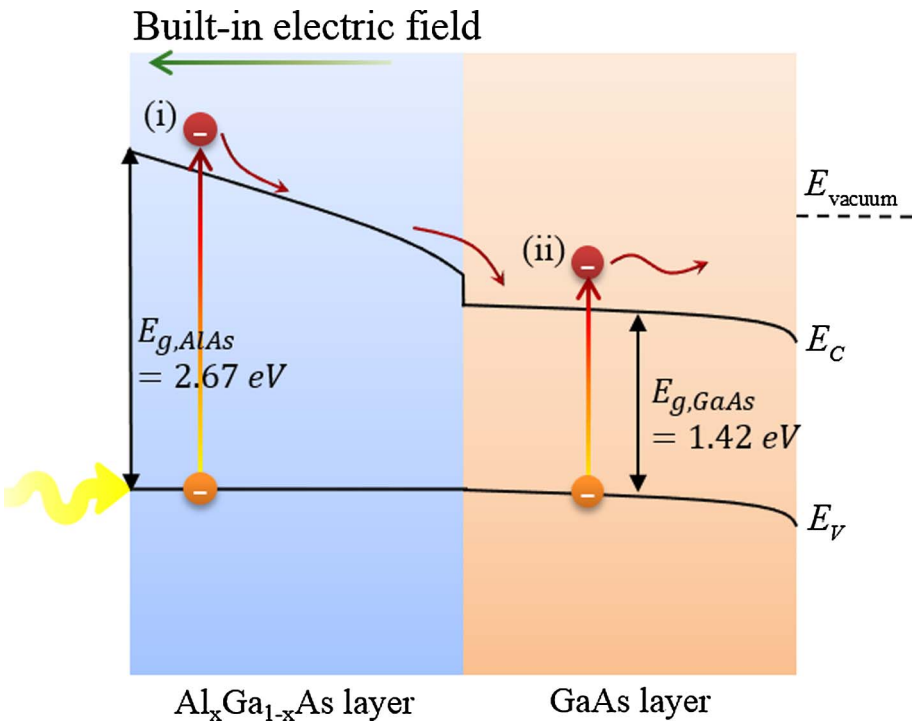

Fig. 9. Schematic band diagram of heterostructure emitter with a graded bandgap window layer. (i) photoexited electrons in $Al_xGa_{1-x}As$ are accelerated by built-in electric field toward the heterostructure, (ii) PETE in GaAs layer.

and collector and can lead to ionization. It has been proposed that the current densities approach the theoretical PETE limits at high excitation fractions. The sudden rise in current is due to the ignition, i.e. the rapid rise in plasma density associated with superelastic heating and runaway ionization [111].

4.2. Negative electron affinity emitter based PETE conversion

Since the successful application of nitrogen-doped H-terminated diamond with a negative electron affinity for heat-induced thermionic conversion, scientists have studied the potential existence of PETE in diamond films. Generally, diamond has a wide bandgap (~5.5 eV @ 300 K) and is transparent to solar photons. Calvani et al. fabricated black diamond via surface texturing by ultrashot pulse laser treatment. It is reported that diamond with 1D periodic surface structure achieved a solar absorptance of > 90%, while that with 2D one has an excellent solar absorptance of 98% [112,113]. A novel two-layer configuration of a nitrogen-doped (n-type) hydrogen-terminated diamond film deposited on a boron-doped ([B] ~ 10^{19} cm^{-3}) single-crystal Si (1 0 0) has been proposed for PETE [114]. The silicon substrate is ideal for absorption of the solar spectrum, and the p-type nature will enable a large increase of the electron quasi-Fermi level. Meanwhile, the NEA n-type diamond film provides a low work function surface with a potentially reduced recombination due to the lack of mobile holes. It is observed that the current intensity increases with increasing photon energy, as expected for photoemission at low temperatures. When the temperature was elevated to ~400 °C, the current fluctuated with the photon energy, which, in contrast, was not observed from diamond films deposited on metal substrates. This phenomenon indicates that photon-enhanced thermionic emission dominated this process rather

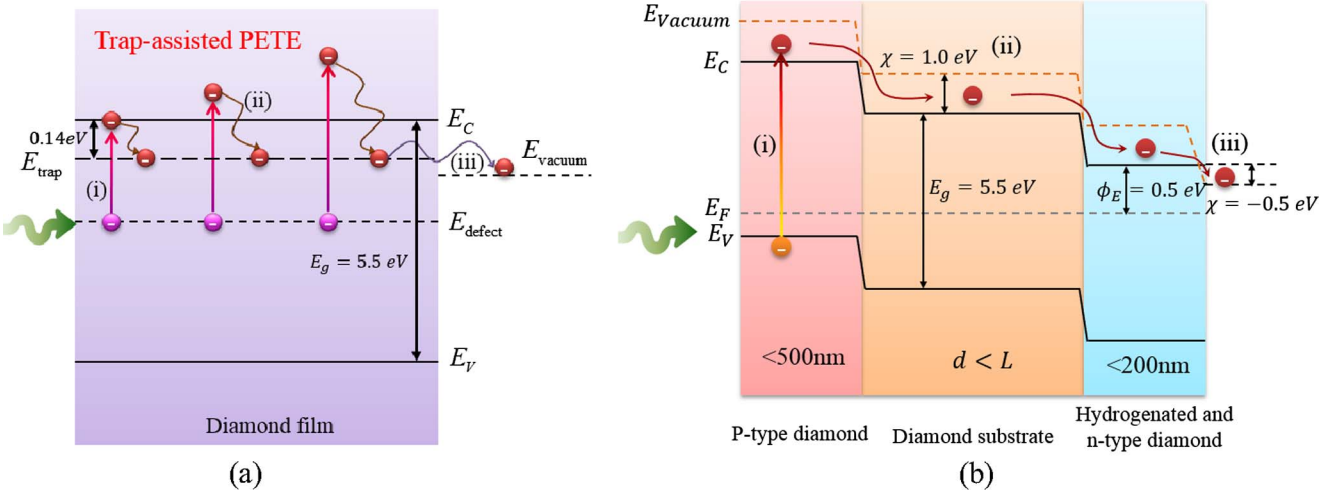

Fig. 10. Schematic illustration of PETE within (a) polycrystalline diamond film, E_{trap} and E_{defect} represents the trapping centers exist below the conduction band minimum and the defect (impurity) level, respectively. (i) photoexcitation of electrons from defect level to the conduction band, (ii) electron–phonon scattering and electron capture by trapping centers, (iii) emission from trap levels into vacuum. (b) surface structured diamond, (i) photoexcitation of electrons into the conduction band just beneath the laser-treated black surface; (ii) diffusion of electrons towards the emitter favored by a depletion of electrons from the surface; (iii) emission into vacuum.

than heat-induced thermionic emission or photoemission. The material is more likely to exhibit PETE if it forms a quasi-equilibrium population of photoexcited electrons. It is reported that the diamonds (both single-crystal and polycrystalline) have electron diffusion lengths of 5–100 μm [115]. However, the thickness of commercially available single-crystal diamond plates is in the range of 300-1200 μm, which results in an extremely high electrical resistivity of bulk diamond ($> 10^{12}$ Ω cm) and thus produces bottlenecks for the emission of current. By laser-writing graphite microchannels as distributed electrodes into the diamond bulk, the cathode series resistance is drastically reduced by $>$ 10 orders of magnitude to a level of 0.75 Ω cm [116].

To understand the nature of nitrogen-doped diamond films for solar thermionic emission, the Nemanich group further investigated the effects of the interface and interlayer on the photoinduced electron generation, transition and emission [117,118,119]. Another three-layer film consisting of a nitrogen-doped diamond layer on the top, a nucleation layer of nitrogen incorporated ultra-nanocrystalline diamond and a molybdenum metal substrate has also been studied for PETE. The nucleation layer could absorb a significant portion of light from ~200 to 900 nm, where the consequent shift of the Fermi level may lead to the filling of in-gap states, and photoelectrons are likely generated from these populated states and then thermalized to a non-equilibrium distribution through phonon scattering. The electronic states of the abundant sp^2 bonds in this layer may result in distinct conductive states that correspond to the additional generation and transmission paths and possibly affect the interface barriers. The effect of PETE within polycrystalline and nanocrystalline diamond films can be explained as a combined three-step process, shown in Fig. 10(a): (i) photoexcited electrons jump from defect level to the conduction band; (ii) electrons are scattered with phonons and captured by trapping centers; and (iii) electrons in the shallow trap levels are thermalized into the vacuum [120]. The dominant recombination mechanism in diamond is the bulk and surface traps [121]. Thus, the excited electrons in the conduction band tend to be captured by bulk or surface trapping centers, which is originated from defects of the grain boundaries [122]. Moreover, Bellucci et al. developed the effect of PETE in single-crystal black-diamond, which is also a 3-step process, but slightly different from the described for polycrystalline films. It can be described as (Fig. 10(b)): (i) photoexcitation of electrons into the conduction band just beneath the laser-treated black surface; (ii) diffusion of electrons towards the emitter favored by a depletion of electrons from the surface; (iii) emission into vacuum [123].

It is found that the diamond emitters show deterioration of their emission properties after ambient exposure or extended operation [124]. The photon enhancement was substantially reduced as the time and temperature increased, which could be related to changes of the interface properties. It is reported that the worsening of interface character can be attributed to the combined effect of the oxidation and hydrogen degradation of emitter surface and the adsorption of contaminants. After the introduction of atomic hydrogen to the emitter, the thermionic emission of the used emitter shows a significant regeneration to a level approaching that of a fresh emitter, which could be ascribed to the reforming of a uniform surface dipole layer. In addition, a new approach has been established to forbid the transition from the sp^3 hybridization to sp^2 hybridization, thus maintaining the performance of the diamond film. This involves methane exposure of the electrodes, where ionization processes occur to compensate the reduced hydrogen atom that is bonded to the carbon surface atom [86].

4.3. All-solid-state PETE conversion

To avoid the complicated fabrication and encapsulation of vacuum photon-enhanced TECs, a novel structure with a semiconductor layer replacing the vacuum gap has been proposed [125], shown in Fig. 11(a). In this configuration, a narrow bandgap intrinsic semiconductor is employed as the photon absorber and wide bandgap doped semiconductor as a material for the two barrier layers. The carriers that are generated in the absorber can be extracted by the hole contact and the electron contact. The conduction band offset of the electron contact was designed as much smaller than the valence band offset. Therefore, the conduction band electrons can easily overcome the barrier for PETE whereas the transportation of valence band holes is blocked. A similar discussion can be made considering the hole transport and the hole contact. It should be noted that the barrier width is less than the mean free path of the carriers in the barrier (i.e., 100 nm) and more than achievable length for electron tunneling (i.e., 10 nm). Calculations show a theoretical conversion efficiency exceeding 30% at temperatures above 327 °C and a flux concentration of 1000.

The aforementioned structure is relatively complicated due to the two barrier layers with different band-edge characteristics. An alternative structure (Fig. 11(b)) with a single GaAs absorber and an AlGaAs barrier layer is proposed [126]. By optimizing the barrier height formed by the band-edge discontinuity, electrons can easily traverse the barrier. An established contrast model shows that the structure with one

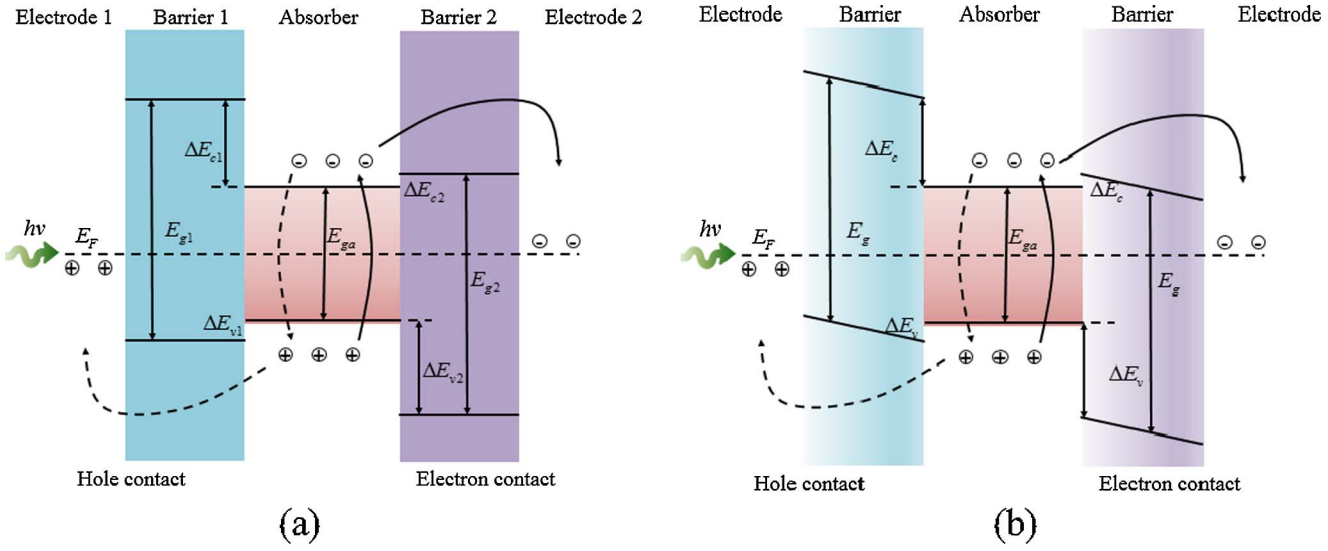

Fig. 11. Band schematics of all-solid-state photon-enhanced TEC, (a) uniform structure; (b) heterostructure. E_{C1} and E_{C2} are the conduction band of barrier 1 and barrier 2, respectively; E_{V1} and E_{V2} represent the valence band of the barrier 1 and barrier 2, respectively; E_{ga}, E_{g1}, E_{g2} are the bandgap of absorber, barrier 1 and barrier 2, respectively, and E_F is the Fermi level.

barrier achieves a higher efficiency than the structure with two barriers in the range of 127–427 °C. According to the theoretical analysis, the front interface recombination has a stronger effect on efficiency than the back interface recombination.

Thermionic emission from planar structures (i.e. smooth interfaces between the barrier and the absorber) is significantly limited by momentum conservation law. Conversely, non-planar structures enable larger thermionic currents, which can be ascribed as the enlargement of interface area for thermionic emission and the reduction of probability of electron reflection at the interface [127].

Another hybrid structure that integrates PETE with electron tunneling was developed to minimize the electron recombination and irreversibility [128]. In this structure, the p-type emitter and n-type collector were separated by sparsely spaced semiconductor nanowires, which confined the electron flow within a windowed energy range. The optimal bandgap of the emitter is reduced to a lower value of 1.15 eV compared to that of the photon-enhanced TEC without electron tunneling. It is calculated that the hybrid converter reached a maximum theoretical efficiency of 51.1% at a solar concentration ratio of 1000.

5. TEC based combined systems

5.1. HITE based combined systems

Heat-induced TECs are suggested as a topping device of power generation systems, such as steam or gas turbine [129,130], combined cycles [131], Stirling engines [132], or thermophotovoltaic [133]. These combined systems are usually employed in the fields of fossil-fired plants [134], nuclear reactors [135], chlorine-caustic plants [136], which will not be expounded in detail in this paper. Moreover, TECs are also applied to solar energy conversion. Ender et al. [137] presented a solar bimodal power system with an overall conversion efficiency of 48.7%, which consists of a high temperature Cs-Ba thermionic energy converter and Alkali Metal Thermal to Electric Converter. Naito et al. [18] designed a combined high-efficiency solar thermionic-thermoelectric conversion system, which is shown in Fig. 12. The thermoelectric converter acts as the heat sink of TEC, and in turn, the waste heat from TEC can be a heat source of the thermoelectric converter, thus increasing the overall theoretical conversion efficiency to approximately 40%. A number of groups have developed several algorithms to provide theoretical guidance for optimization of practical thermionic-thermoelectric hybrid systems [38,138,139]. It has been concluded that the voltage output, the work functions of both electrodes and the electric current of the thermoelectric stage have significant influences on the power output and overall conversion efficiency.

On the other hand, thermionic energy converters can be the bottoming device for waste heat recovery. Huang et al. established a new hybrid system consisting of an internal reforming molten carbonate fuel cell and a TEC. It is found that the maximum power density output of this hybrid system increases by 22% compared to that of a single molten carbonated fuel cell [140]. Fitzpatrick et al. proposed a cascaded thermionic converter comprised of a barium-cesium upper stage and a cesium close-spaced lower stage, which was used for nuclear reactor and achieved a conversion efficiency of 29.2% [135].

5.2. PETE based combined systems

Although PETE exhibits an excellent theoretical performance for solar energy conversion, as described above, its potential value is in the creation of a tandem cycle with a heat converter [141]. Table 6 shows several simulations on the efficiencies and key parameters for tandem systems with a photon-enhanced TEC.

5.2.1. Front-illuminated configuration

Currently, the vast majority of photon-enhanced TECs have front-illuminated configurations, whose schematic diagram is shown in Fig. 13. This configuration is beneficial for a convenient implementation, the easy introduction and absorption of sunlight and the controllable management of the temperature difference between the emitter and collector. Unlike heat-induced thermionic conversion, photon-enhanced thermionic conversion allows photons that are not absorbed in the emitter to propagate and heat up the collector. This could increase the overall efficiency when the second heat generator

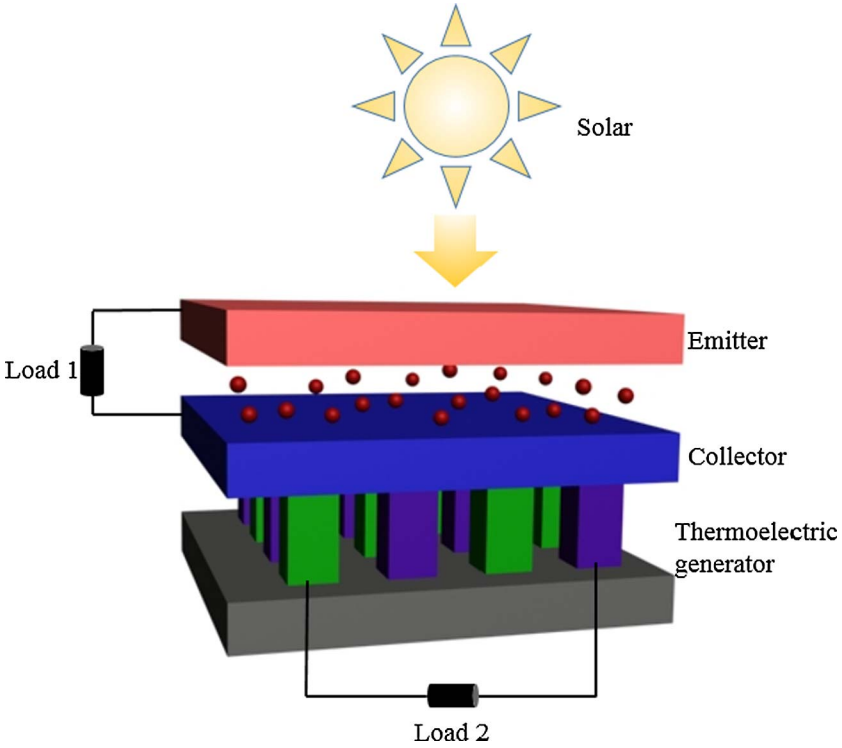

Fig. 12. Schematic diagram of the TEC-thermoelectric hybrid system.

Table 6
Numerical simulations on PETE systems with second thermal converters.

Author (year)	Description	E_g (eV)	χ (eV)	ϕ (eV)	T_E (°C)	T_C (°C)	η_{PETE}	$\eta_{Thermal}$	η_{Total}
Schwede (2010) [15]	Original numerical simulation of PETE	1.15	1.0	0.9	800	285	37.9%	31.5%	52.9%
Segev (2013) [142]	Side illuminated, series connected PETE device with second thermal cycle	1.38	0	0.9	537	537	27.0%	60% of Carnot efficiency	52.0%
Reck (2014) [143]	Introducing analytic thermodynamics model	0.56	1.34	0.41	1178	55	55.2%	Carnot efficiency	58.0%
Su (2014) [23]	PETE/thermoelectric hybrid system	1.21	1.14	0.9	960	312	42.2%	Practical efficiency of thermoelectric generator	45.7%
Segev (2015) [144]	Single bandgap, side illuminated PETE device with second thermal cycle	1.4	0.4	0.9	427	427	24.7%	Carnot efficiency	69.8%
Segev (2015) [144]	Single bandgap, front illuminated PETE device with second thermal cycle	1.4	0.4	0.9	1022	227	52.1%	Carnot efficiency	63.0%
Segev (2015) [144]	Dual bandgap, thermally coupled PETE device with second thermal cycle	1.8 and 1.185	0.4	0.9	883	227	56.3%	Carnot efficiency	70.4%
Segev (2015) [144]	Dual bandgap, thermally isolated PETE device with second thermal cycle	1.85 and 1.15	0.4	0.9	1274 and 876	227	54.3%	Carnot efficiency	69.0%

E_g and χ represent the bandgap and electron affinity of the emitter, respectively, ϕ is the work function of the collector, T_E and T_C are the temperatures of the emitter and collector, respectively, C represents the concentration ratio, η_{PETE} is the conversion efficiency of PETE only, $\eta_{Thermal}$ is the conversion efficiency of secondary thermal cycle, and η_{Total} is the total conversion efficiency of the combined system with the second thermal converter. All the works were conducted with a concentration ratio of 1000.

dominates the photon-enhanced TEC. Schwede et al. predicted that a tandem conversion efficiency of a PETE-steam turbine exceeds 52.9% at a concentration of 1000 suns, which constitutes a 40% increase over that of a photon-enhanced TEC alone. By analyzing the entropy production of the PETE process, Reck et al. evaluated the maximum efficiency of the PETE system with a secondary thermal stage as up to 58.0%, which is higher than that of the PETE device alone [143].

Another PETE hybrid system with a thermoelectric generator was designed by Su et al. [23]. The configuration is composed of a photon-enhanced TEC on the top and a series-connected thermoelectric generator attached to the collector electrode of the photon-enhanced TEC. It is claimed that the bandgap and the electron affinity of photon-enhanced TEC can dramatically change the overall output and conversion efficiency. According to the hybrid model established, an overall maximum efficiency of 45.7% is obtained with an emitter's bandgap of 1.21 eV, which deviates from the bandgap of 1.38 eV for the optimal photon-enhanced TEC alone.

Similar to photovoltaic cells, the conversion efficiency of the photon-enhanced TEC can be increased via spectral splitting [144,145,146]. Fig. 14(a) shows a dual-bandgap photon-enhanced TECs, where two sub-devices are optically parallel and electrically independent. Fig. 14(b) shows an alternate configuration, where two sub-devices are connected in series, both optically and electrically. It is stated that the latter configuration has a lower optical efficiency due to impedance mismatch in the semiconductor-vacuum interfaces. For the first configuration, the overall efficiency of the PETE-thermal engine can approach 70.4% when the two PETE sub-devices are thermally coupled with an equal temperature, while a total system efficiency of 69.0% was predicted with the isolated PETE sub-devices. It is noted that the enhancement due to spectral splitting is lower as compared to that of photovoltaics. This can be attributed to the lower operation temperature in the dual-bandgap photon-enhanced TEC due to spectral splitting compared to that in the single-bandgap converter, which results in reduced thermalization energy for electron emission.

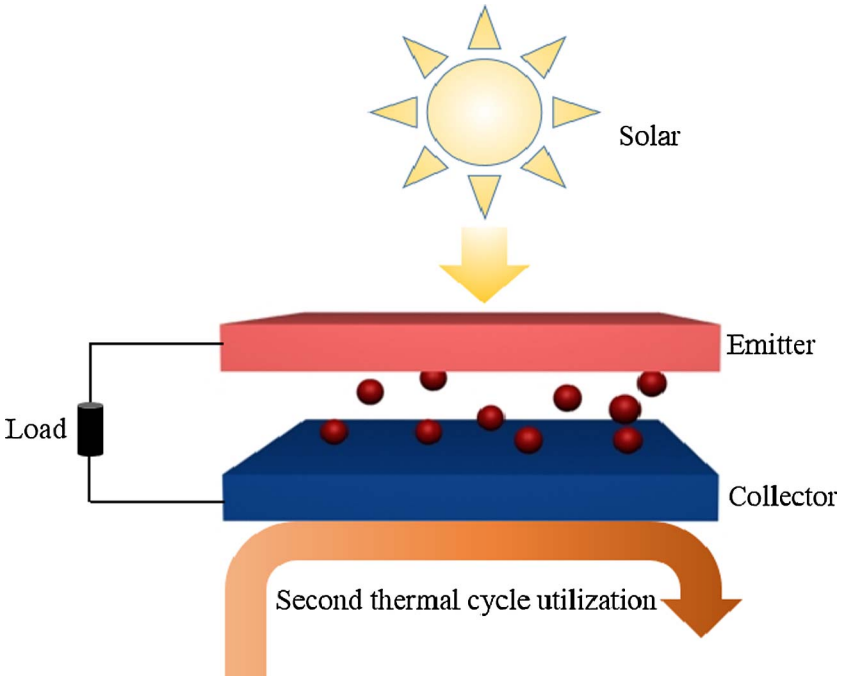

Fig. 13. Schematic diagram of tandem system with the front-illuminated photon-enhanced TEC.

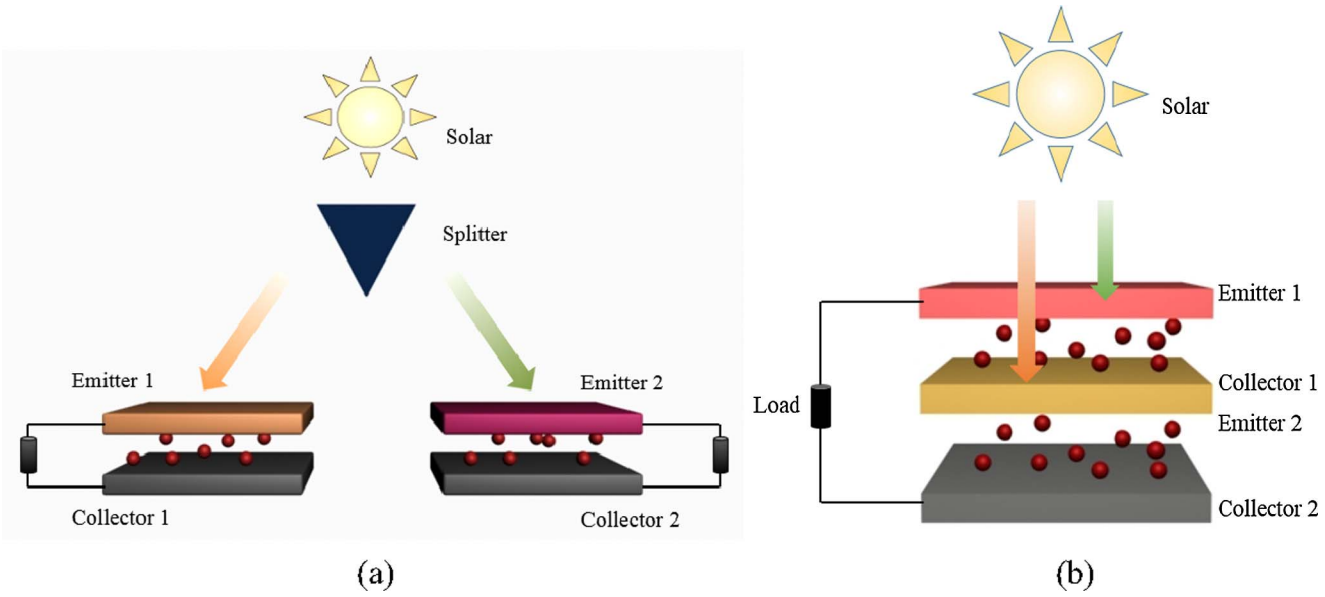

Fig. 14. Schematic diagrams of two types of dual-bandgap photon-enhanced TECs, (a) optically connected in parallel and (b) optically connected in series.

5.2.2. Side-illuminated configuration

Unlike heat-induced TECs, the photon-enhanced TECs have the ability to transform solar radiation into power even when the emitter and collector are isothermal, which occurs in the side-illuminated configuration. The schematic of this novel configuration is shown in Fig. 15(a), where the surface for receiving sunlight and the surface for emitting electrons are orthogonal [147]. In this case, the population of electrons photo-thermally generated in the emitter is equivalent to that of the collector, by supposing that both the emitter and the collector have the same semiconducting structure. However, the photoelectrons, which are only generated in the emitter, can be emitted into vacuum and produce electricity due to a low electron affinity coating. As a result, the power conversion is actuated only by the photoelectric effect and is independent of temperature. The efficiency is strictly constrained by the Shockley-Queisser limit due to the additional thermalization loss from the collector and the high radiative recombination [148].

From the perspective of the tandem system with a thermal cycle, the side-illuminated configuration may be superior to the front-illuminated configuration [149]. For the front-illuminated configuration, the secondary thermal converter is connected to the collector, so the heat transferred to it depends on the work function of the collector for the optimum overall efficiency. On the other hand, for the side-illuminated configuration, waste heat is extracted from both electrodes. The effect of collector work function on efficiency is accordingly reduced. It is interesting to note that the side-illuminated photon-enhanced TEC, while may offer a lower efficiency in an individual configuration, can surpass the front-illuminated one in some cases when combined with a second thermal cycle [144].

In order to obtain high power outputs, a novel configuration (shown in Fig. 15(b)) was proposed, where photon-enhanced TECs are electrically connected in series and thus the voltage and power output are multiplied [142]. Unlike the top-to-bottom connection, the parallel

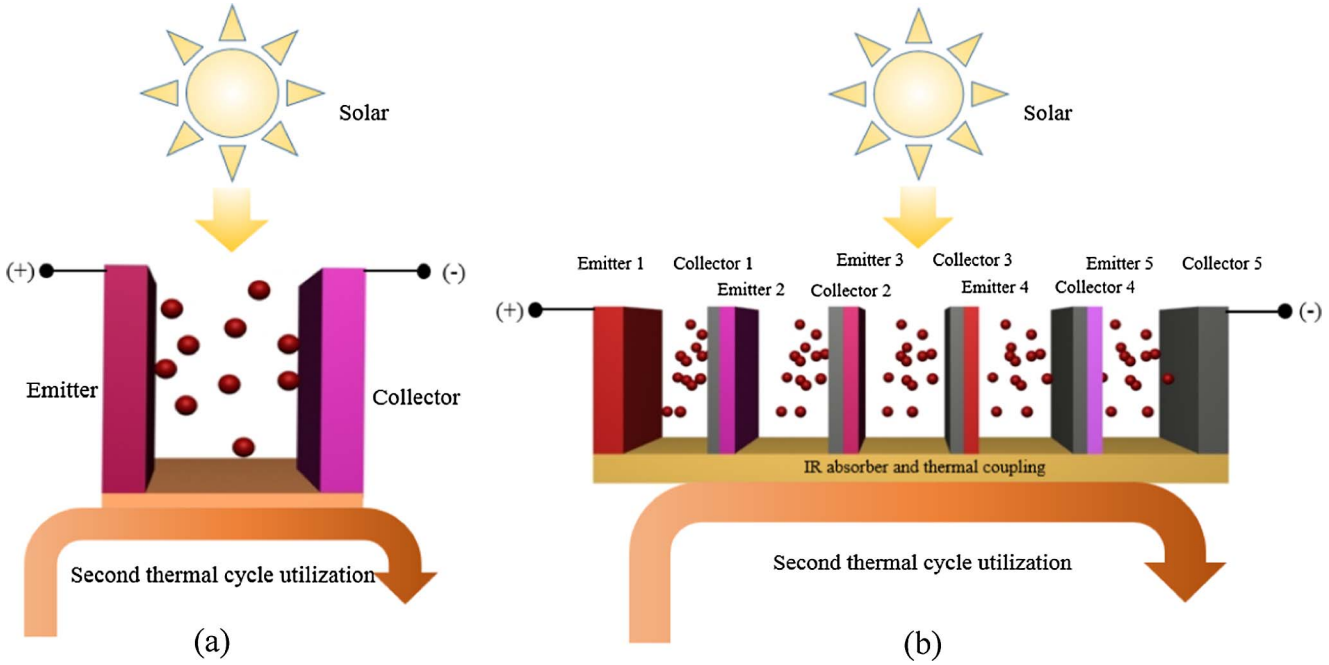

Fig. 15. Schematic diagram of tandem system with the side-illuminated photon-enhanced TEC. (a) one converter; (b) converters connected in series.

allocation in the side-illuminated configuration does not require redundant area to function and prevents an overall increase of in the Ohmic resistance. According to the description in [147], the collector of the preceding emitter–collector pairs is the electrical contact to the subsequent emitter. An electron blocking layer should be established at the collector-emitter interface to inhibit surface recombination at the contact. It is proposed that a p^+p junction heterostructure or an accumulative metal–semiconductor contact is an effective candidate for this purpose [32].

6. Discussion of practical TEC based CSP

Thermionic energy conversion is suitable for both small-scale and large-scale in various kinds of applications, e.g. space exploration and solar power plant. As to space exploration, power source should be characterized by high compactness (> 100 W/kg), high power output (10–100 kW) and long lifetime (> 5 years) [150]. A solar thermionic system can offer advantages in terms of stowed payload volume and mass with a power ranging from several kilowatts to tens of kilowatts. A novel inflatable solar concentrator was used in HPALM program [13], which can reduce the overall weight of the thermionic system. It is reported that the HPALM thermionic system had a higher specific mass and specific volume than PV cells, i.e. 106 W/kg vs. 60 W/kg and 80 kW/m^3 vs. 4 kW/m^3, respectively [13]. The lifetime of thermionic system varies with different electrode materials, operation temperatures and structure configurations. It is worth noting that the out-core thermionic system, which was operated in nuclear reactor, survived for 75000 h, while the in-core one deteriorated after 20000 h operation [151].

6.1. Practical compatibility

Thermionic energy conversion is a potential option to combine with CSP technologies, where higher temperature means higher efficiency, unlike photovoltaic (PV) or concentrating photovoltaic (CPV). Solar thermionic systems can be used for remote residences, apartment house complexes and large central power stations [152]. A typical solar thermionic power plant consists of solar concentrators, concentrator tracking drive and control subsystem, power processing subsystem, thermionic converter modules (located at the focal point of solar concentrator) and bottoming heat engines, as shown in Fig. 16.

There are five main categories of solar concentrators, i.e. heliostat field reflectors, parabolic dish reflectors, parabolic trough reflectors, linear Fresnel reflectors and Fresnel lenses, as listed in Table 7. The heliostat field type, as shown in Fig. 17(a), features a large amount of plane or slightly curved mirrors which are distributed around a central solar tower and reflect light onto the top of the tower. Generally, this kind of solar concentrator can approach a concentration ratio of up to 1000 suns for a high temperature receiver (e.g. chemical reactor, particle receiver or thermionic energy converter) at up to 1400 °C, and usually it has the maximum power scale compared to the other kinds of concentrators, usually ranging from 5 MW to 200 MW. A parabolic dish reflector can reach an operation temperature of up to 2000 °C with a concentration ratio of up to 3000 suns [153]. A TEC can be mounted at the focal point of a parabolic dish reflector, shown in Fig. 17(b). For a single dish system is usually 1 kW to 100 kW. Parabolic troughs and linear Fresnels are usually called linearly concentrating method, whose concentration ratio is usually 40–100 suns, These concentrators are not practically suitable for thermionic energy conversion because of the low operating temperature. Fresnel lens (seen in Fig. 17(c)) is widespread apparatus for concentrating solar radiation in small scale (1–1000 W) [154]. Han et al. [155] reported a two-stage system, consisting of a front Fresnel lens and a second stage compound parabolic concentrator, reaching a concentration ratio of over 1000 suns. The losses of concentrator are mainly determined by tracking error, mirror reflectivity (or lens transmissivity). It is reported that the concentration ratio decrease from 2000 to 400 when the tracking error increases from 0.2° to 0.5° [152], which can reduce the receiver temperature and increase intercept loss. The losses due to cosine efficiency, blocking and shading should also be taken into account when heliostat field is chosen. In the process of receiving solar radiation, convective, emissive, reflective and conductive losses are contributed to the total heat losses. A collection efficiency of 74% and collection thermal power of 69 kW (93 kW incident solar radiation) can be obtained when the glass reflectivity is

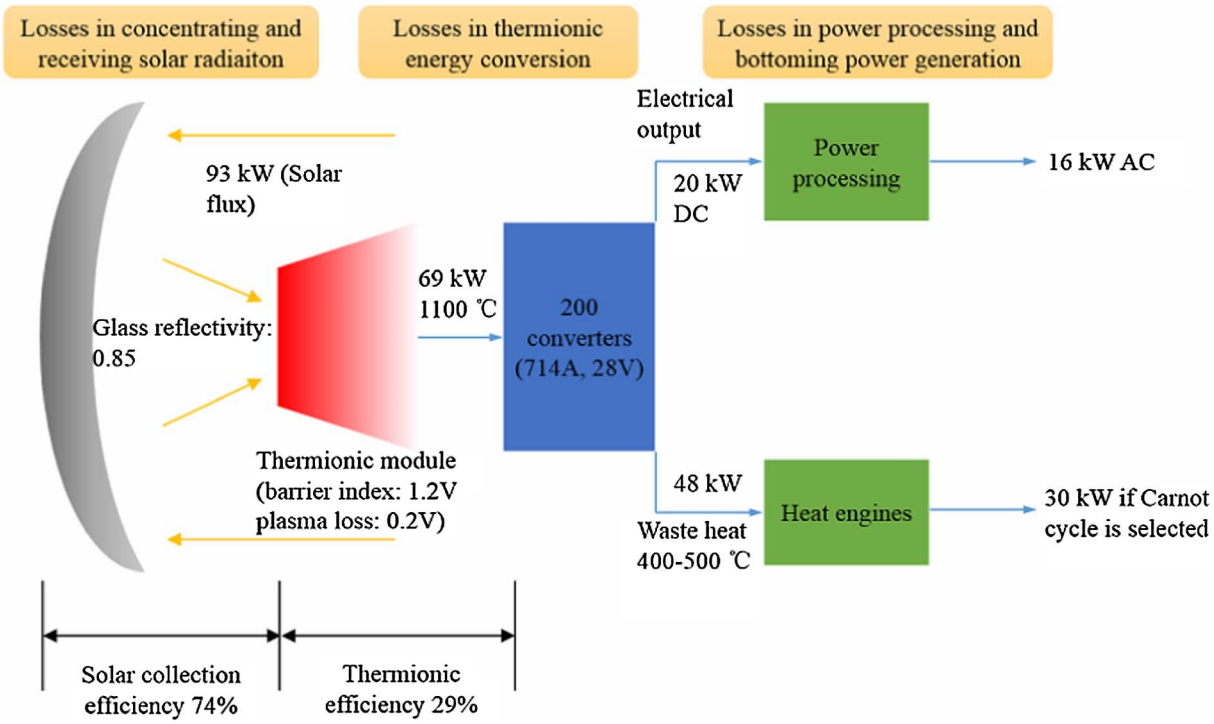

Fig. 16. Schematic of a planned solar thermionic power generation [152].

Table 7
Solar concentrators for TECs [153,156].

Concentrator type	Scale	Typical emitter temperature (°C)	Concentration ratio (suns)	Description	Practically Suitable or not
Heliostat field reflectors	5–200 MW	500–1400	300–1000	Large amount of heliostat reflectors guides sunlight to the upside of solar tower	Yes
Parabolic dish reflectors	1–100 kW	500–2000	500–3000	The focal point and parabolic dish reflector moves with the sun	Yes
Parabolic trough reflectors	/	350–550	50–80	The concentration ratio of the focal line of parabolic trough reflectors is not high enough	No
Linear Fresnel reflectors	/	270–550	25–100		No
Fresnel lenses	1–1000 W	400–1000	100–1000	Solar radiation is transmitted through Fresnel lens and concentrate on the focal area	Yes

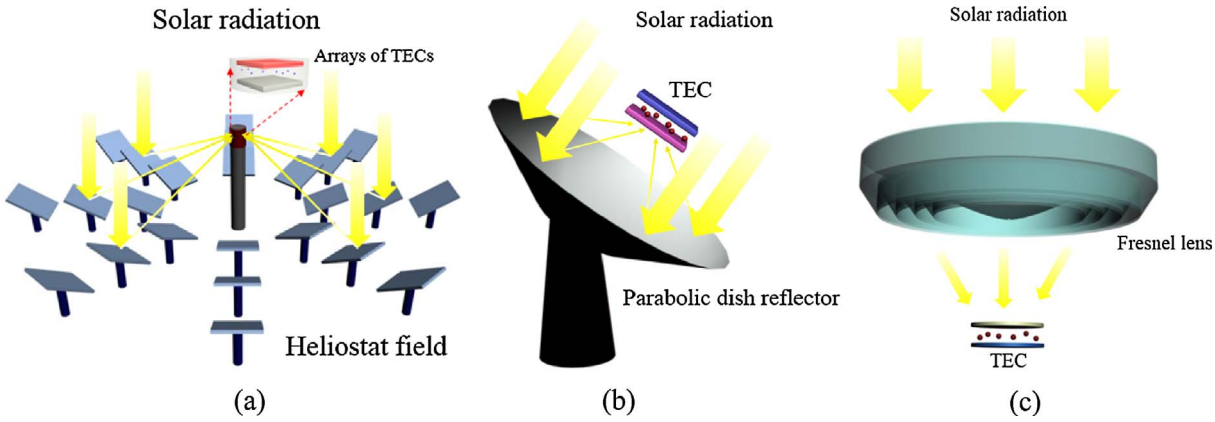

Fig. 17. Schematic of TECs applied in (a) heliostat field system, (b) parabolic dish reflector and (c) Fresnel lens system.

assumed to be 0.85 and the cavity absorptivity and emissivity are 1.0, respectively [152].

The losses in thermionic energy conversion is mostly due to the irreversibilities of electron transportation. Space charge effect is merely inevitable and causes significant loss in the interelectrode space, though an amount of methods were developed for mitigating space charge effect. A thermionic efficiency of 29% and DC output of 20 kW is possible if the barrier index and plasma loss are assumed to be 1.2 V and 0.2 V, respectively. After power processing with a boost regulator, the AC output decreases to 16 kW [152]. Moreover, the non-uniform heat flux can cause a 20–40% drop in array output power as compared to a case with uniform heat input [157].

In the case of HITE, the emitter is usually over 1400 °C and the collector electrode operates at 500–1000 °C. While in the case of PETE, the temperature of the emitter is in the range of 400–1200 °C and the collector generally runs at 300–600 °C. It is worth noting that the temperature of collector is high enough to drive a bottoming thermal cycle, e.g. conventional heat engines, to improve the total efficiency of the whole system. Three practical thermal cycles, i.e. Stirling, Rankine and Brayton cycles, are potential options for bottoming thermal utilization, and their characteristics are listed in Table 8.

Stirling cycle, in which a compressible fluid such as helium or hydrogen reciprocates in the engine, can be run with relatively low temperatures of 400-800 °C [158]. A principally schematic configuration of TEC combined with Stirling engine is shown in Fig. 18(a), where a heat sink of TEC is connected to a heater of Stirling engine. Stirling engine is an optimal candidate for bottoming thermal utilization in small scale (1–100 kW_e). Rankine cycle,as shown in Fig. 18(b), where two phase working fluids exist during a operation cycle, exhibits particular potentials for bottoming thermal utilization [160,161], where the typical ranges of thermal power and operating temperature of an organic Rankine cycle are 100 kW-10 MW and 80–300 °C, respectively, whereas for a normal (steam) Rankine cycle they are 10 MW-1GW and 400–600 °C. A principle configuration of TEC-Brayton hybrid system is shown in Fig. 18(c), where working fluid passes through a compressor and a regenerator, absorbs heat from TEC, and subsequently expands in

Table 8
Potential bottoming thermal cycles.

Bottoming thermal cycle	Practical heat engines	Typical temperatures of residual heat (°C)	Typical thermal power	Typical thermal efficiency	Working medium	Characteristics
Stirling cycle [158,159]	Stirling engine	400–800	1–100 kW	~40%	Helium, Hydrogen, or Nitrogen	Reciprocating motion of gas
Rankine cycle [160,161]	Organic Rankine cycle	80–300	100 kW–10 MW	7%-20%	Organic compound such as refrigerants and hydrocarbons	Two phase working fluids
	Steam turbine	400–600	10 MW–1 GW	~35%	Water	
Brayton cycle [162]	Supercritical CO_2 cycle	500–700	> 10 MW	~50%	CO_2	Single phase working fluid
	gas turbine	> 800	5 kW–100 kW 1 MW–20 MW 100 MW–500 MW	~30%	Air, flue	

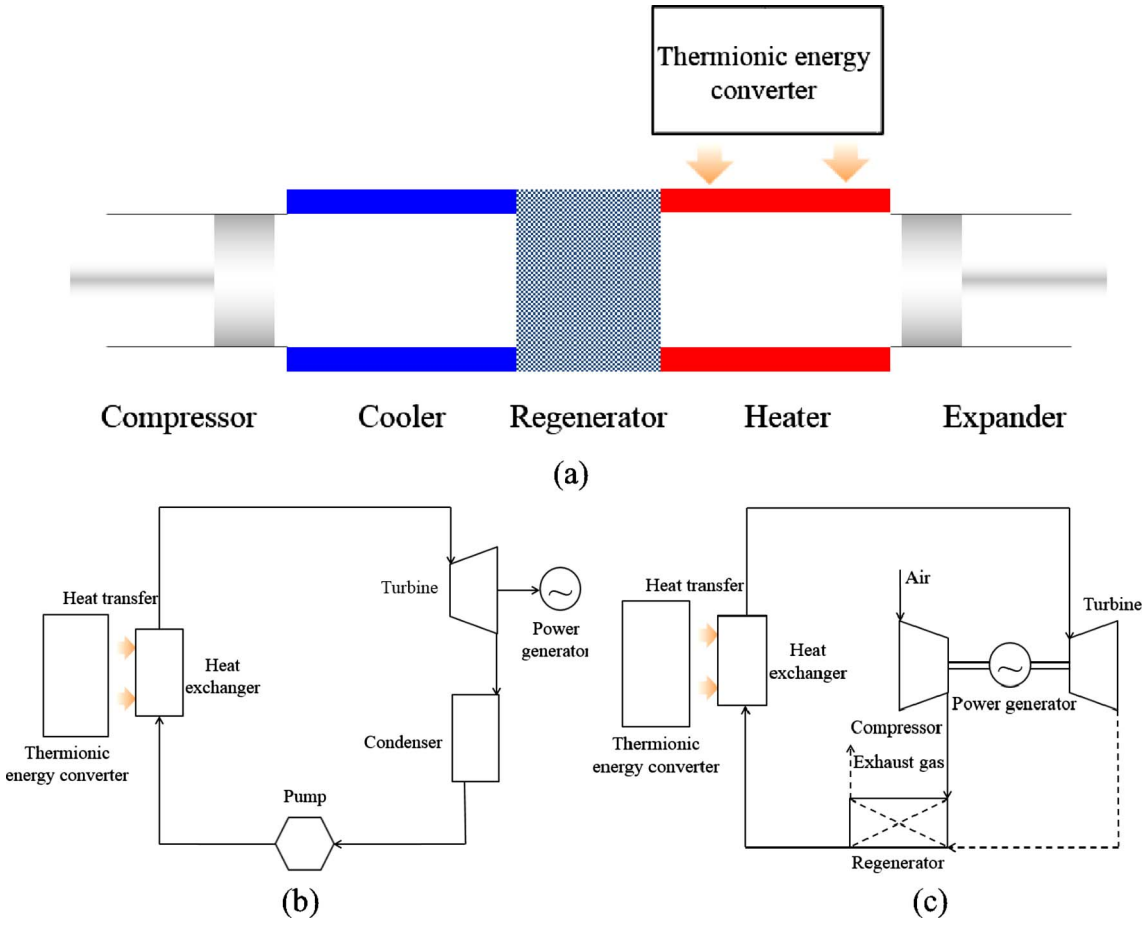

Fig. 18. Principle configurations of TEC combined with (a) Stirling cycle; (b) Rankine cycle and (c) Brayton cycle.

a turbine to generate power [162]. It is noted that Brayton cycle requires a high operation temperature (500–700 °C for Supercritical CO_2 and > 800 °C for air or flue.

Cost is one of the most dominate factors for developing power sources. Generally, the higher the total power output is, the lower the specific cost becomes. Taking a terrestrial solar thermionic power plant as an example [152], the total specific cost is as high as 3033 $/kWe for 1 MW rating. However, it decreases to 1052 $/kWe when the peak plant rating is 1000 MW [152]. There are reasons to believe that the modern technologies can probably reduce the price according to the price change of PV in the past forty years, shown in Fig. 19 [163].

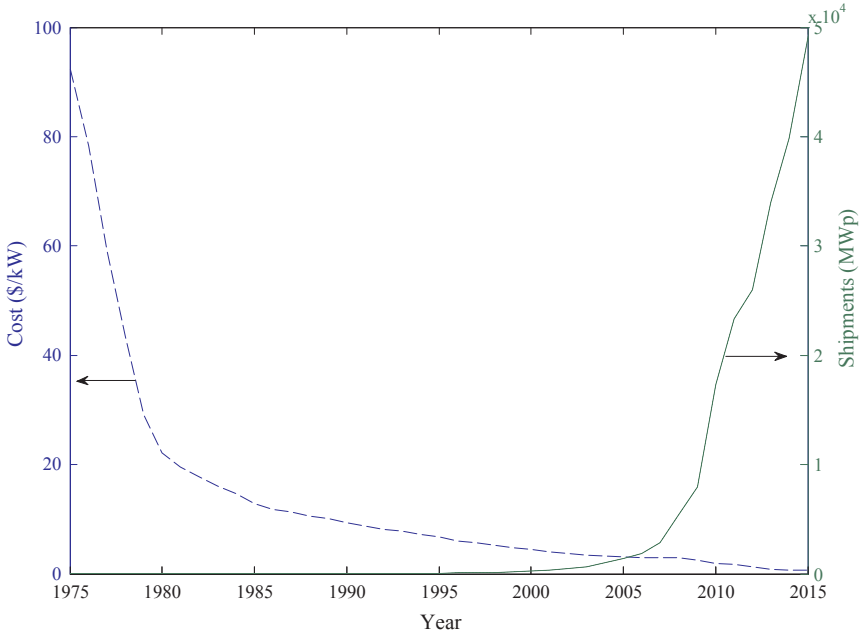

Fig. 19. PV module price sand shipments from 1975 to 2015 [163].

6.2. Thermodynamic analysis

As to conventional CSP systems, concentrated solar radiation is firstly absorbed by a receiver, then thermal energy is transferred to working medium, e.g. pressured steam, gas or organic materials, and is finally converted into work in an engine or turbine. As to a TEC based CSP system, besides a conventional bottoming thermal cycle, a thermionic energy conversion process can be featured in temperature-entropy diagram [164,165,166], shown in Fig. 20(a). In branch 1 → 2, the whole process of electron emission is related to an entropy production.

$$\Delta S_{12} = \frac{J_{em}(\phi_E + 2kT_E) - J_{rev}(\phi_E + 2kT_C)}{qT_E} \tag{17}$$

Branch2 → 3 represents a transport process of electron in the gap, where the excess electron kinetic energy is irreversibly deposited as heat at the collector, and the entropy change is

$$\Delta S_{23} = \frac{(J_{em}\phi_E - J_{rev}\phi_C)(T_E - T_C)}{T_E T_C} \tag{18}$$

In branch 3 → 4, the energy carried by the electron stream is rejected as heat, resulting in the thrmalization of electrons to the Fermi level of the collector electrode. The entropy change in this process is

$$\Delta S_{34} = \frac{J_{em}(\phi_C + 2kT_E) - J_{rev}(\phi_C + 2kT_C)}{qT_C} \tag{19}$$

Due to the difference of electron concentration, electrons in the collector are channeled back to the emitter via the lead wire. For simplicity, the irreversibilities of resistive and thermal conduction losses are ignored (e.g. in the case of super-conductive leads), thus no entropy change is assumed in the branch 4 → 1.

As to a TEC combined with a heat engine, the thermal energy deposited from the TEC represented by the quantity Q_{34} is assumed to equal to the input of the heat engine with a perfect heat exchanger, namely, the temperature of collector in TEC is equal to that of heater of the heat engine. Here, three practical bottoming cycles, i.e. Stirling, Rankine and Brayton, are discussed, and simply combined temperature-entropy diagrams are illuminated in Fig. 20(b), (c) and (d), respectively. It is noted that multiple bottoming cycles can be deduced further, which are not discussed here.

As discussed above, PETE exhibits a better performance compared to HITE because of better absorption for concentrating sunlight and higher theoretical maximum energy conversion efficiency. Fig. 21(a) compares the efficiencies of HITE and PETE in the assumptions that the concentration ratio is 1000 suns [15], the emitter is 10^{19} cm^{-3} p-type doped semiconductor with a band gap and electron affinity of 1.5 and 1.0 eV, respectively, the thickness of the emitter is 2 μm and the work function of the collector is 1.2 eV. Fig. 21(b), (c) and (d) display the overall efficiencies of combined systems, i.e. HITE or PETE combined with an ideally thermal bottoming cycles respectively, where the thermal power is totally converted to electricity. Generally, the theoretically overall efficiency of HITE-Stirling or PETE-Stirling systems are higher than other combining modes, about two times of that of simple

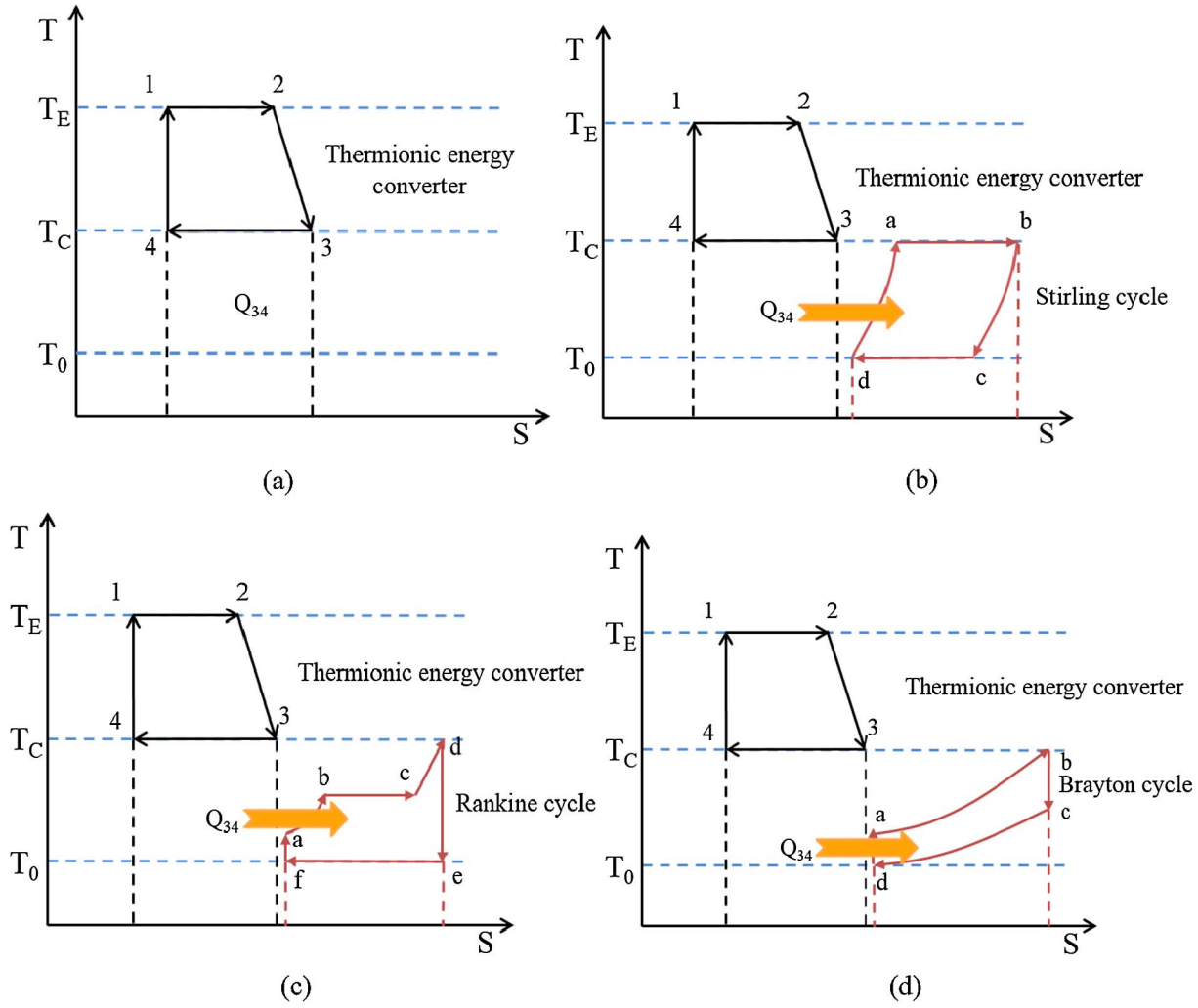

Fig. 20. The temperature-entropy diagrams of (a) TEC alone; (b) TEC-Stirling hybrid system; (c) TEC-Rankine hybrid system and (d) TEC-Brayton hybrid system.

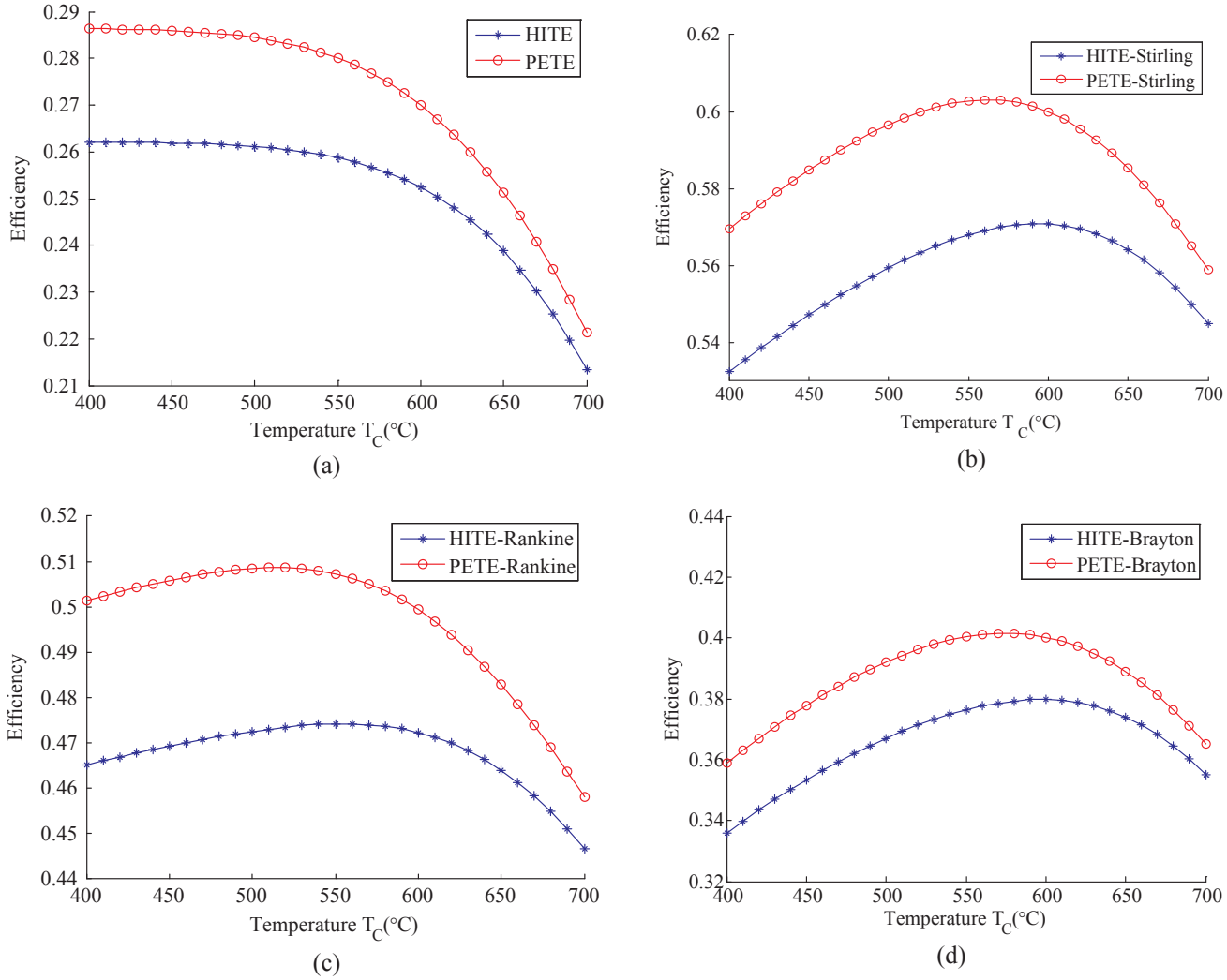

Fig. 21. The comparative efficiency of (a) HITE and PETE alone; (b) HITE-Stirling and PETE-Stirling hybrid systems; (c) HITE-Rankine and PETE-Rankine hybrid systems and (d) HITE-Brayton and PETE-Brayton hybrid systems.

HITE or PETE, respectively, and the peak overall efficiencies occur when the temperature of collector (Tc) is in a range of 500–600 °C no matter which kind of bottom cycle is combined with. It indicates that a practically potential bottoming cycle is the one having a good efficiency at 500–600 °C in this case. Thus, Stirling and Ranking cycles are practical options. Stirling cycle is suggested to work with small scale systems of 1–100 kW [159], while Ranking cycle is suggested for large scale systems of over 10 MW [167]. As to middle scale systems of 100 kW to 10 MW, organic Ranking cycle is probably an option, and it is worth noting that the highest operation temperature is generally less than 300 °C now [168]. Conventional Brayton cycle is not an option to combine with TEC based CSP, because the working temperature is always higher than 800 °C, but supercritical CO_2 Brayton cycle is probably a potential option, which has an efficiency of about 50% at 500–600 °C [163].

7. Conclusions

An overview of thermionic energy conversion for CSP is presented in this paper. The review includes the fundamental principles of solar thermionic energy conversion, the state of the art of solar thermionic technologies covering heat-induced and photon-enhanced thermionics, as well as the practical TEC based CSP combined cycles. The overall literature refers to the energy conversion efficiency of TEC and summarizes the methods to enhance the conversion efficiency both in HITE and PETE systems.

- As for heat-induced solar thermionics, some prototype converters were established with energy conversion efficiencies of 7–23%. Main research hotspots to improve energy conversion efficiency are enhancing thermionic emission at the emitter, reducing space charge effect in the interelectrode gap and optimizing the collector electrode. With regards to enhancing the thermionic emission, the main aims refer to lowering work function of the emitter. Several methods, i.e. depositing low work function materials onto the emitter, micro/nanostructure geometry engineering of the emitter surface and introducing novel carbon based nanomaterials, have been proposed. As for space charge effect mitigation, four critical methods, i.e., introducing cesium into the interelectrode gap, employing NEA electrode, electrostatic triode configuration and molecular assisted charge transport of electrons, are put forward. The optimum management of temperature and surface morphology of the collector are the main ways for optimization of the collector.
- Photon-enhanced TEC exhibits a theoretical energy conversion efficiency of up to 43%. A main research hotspot is to prepare appropriate emitter materials for enhancing photon absorption and electron quantum yield. Plasmonic nanostructure and spectral splitting are suggested for enhancing photon absorption of the emitter. On the other hand, positive electron affinity emitters (e.g., $Al_xGa_{1-x}As$/GaAs, Si, InP) and negative electron affinity emitters

(e.g., diamond) are well appropriated and widely researched for PETE, owing to the optimal bandgap and high quantum yield of III-V semiconductors, and the high temperature stability, combined with excellent emission properties, of diamond.

- As for TEC based CSP, except for the thermionic/thermoelectric and thermionic/photovoltaic tandem systems, the theoretically overall efficiency of combined thermal cycles can approach 60%. The PETE combined systems achieve the optimal efficiencies at a lower collector temperature if compared to HITE combined systems. An optimal overall efficiency of 60.3% is predicted for PETE-Stirling system at a collector temperature of 560 °C, while 50.9% was obtained for PETE-Rankine system at 510 °C and 40.2% for PETE-Brayton at 570 °C, respectively. For small scale systems, parabolic dish concentrators and bottoming Stirling cycles are suggested, and heliostats field collectors and bottoming steam Rankine cycle are suggested for large scale systems. After all, supercritical CO_2 Brayton cycle is a potential option in the future.

Acknowledgements

The authors gratefully acknowledge the supports from the National Key Research and Development Program of China (No. 2017YFA0205700 and No. 2016YFE0124700).

References

[1] Technology roadmap: solar photovoltaic energy. International Energy Association; 2014.
[2] Technology roadmap: solar thermal electricity. International Energy Association; 2014.
[3] Lovegrove K, Stein W. Concentrating solar power technology: principles, developments and applications. Elsevier; 2012.
[4] Sonneveld PJ, Swinkels G, Van Tuijl BAJ, et al. Performance of a concentrated photovoltaic energy system with static linear Fresnel lenses. Sol Energy 2011;85(3):432–42.
[5] Segal A, Epstein M, Yogev A. Hybrid concentrated photovoltaic and thermal power conversion at different spectral bands. Sol Energy 2004;76(5):591–601.
[6] Baig H, Heasman KC, Mallick TK. Non-uniform illumination in concentrating solar cells. Renew Sustain Energy Rev 2012;16(8):5890–909.
[7] Weinstein LA, Loomis J, Bhatia B, et al. Concentrating solar power. Chem Rev 2015;115(23):12797–838.
[8] Mills DR, Morrison GL. Compact linear Fresnel reflector solar thermal power plants. Solar energy 2000;68(3):263–83.
[9] Baranowski LL, Snyder GJ, Toberer ES. Concentrated solar thermoelectric generators. Energy Environ Sci 2012;5(10):9055–67.
[10] Meir S, Stephanos C, Geballe TH, et al. Highly-efficient thermoelectronic conversion of solar energy and heat into electric power. J Renew Sustain Energy 2013;5(4):043127.
[11] Khoshaman AH, Fan HDE, Koch AT, et al. Thermionics, thermoelectrics, and nanotechnology: New possibilities for old Ideas. IEEE Nanatechnol Mag 2014;8(2):4–15.
[12] Hatsopoulos GN, Gyftopoulos EP. Thermionic energy conversion, vol I: processes and devices; 1973.
[13] Streckert H, Peltier D, Begg L, et al. Conceptual design of high power advanced low mass (HPALM) solar thermionic power system. In: El-Genk MS, Bragg MJ, editors. AIP conference proceedings, vol. 608, no. 1. AIP; 2002, p. 1028–36.
[14] Smestad GP. Conversion of heat and light simultaneously using a vacuum photodiode and the thermionic and photoelectric effects. Sol Energy Mater Sol Cells 2004;82(1):227–40.
[15] Schwede JW, Bargatin I, Riley DC, et al. Photon-enhanced thermionic emission for solar concentrator systems. Nat Mater 2010;9(9):762–7.
[16] Houston JM, Webster HJ. Thermionic energy conversion. Adv Electron ELectron Phys 1963;17:125–206.
[17] Rouklove P. Thermionic converter and generator development. Space Programs; (United States), 1966, 4.
[18] Naito H, Kohsaka Y, Cooke D, et al. Development of a solar receiver for a high-efficiency thermionic/thermoelectric conversion system. Sol Energy 1996;58(4–6):191–5.
[19] Shimizu M, Eguchi K, Itoh K, et al. JSUS solar thermal thruster and its integration with thermionic power converter. In: El-Genk MS, Bragg MJ, editors. AIP conference proceedings, vol. 420, no. 1, AIP; 1998, p. 364–9.
[20] Clark PN, Desplat JL, Streckert HH, et al. Solar thermionic test in a thermal receiver. In: El-Genk MS, editor. AIP conference proceedings. vol. 813, no. 1, AIP; 2006, p. 598–606.
[21] Yaghoobi P, Moghaddam MV, Nojeh A. "Heat trap": Light-induced localized heating and thermionic electron emission from carbon nanotube arrays. Solid State Commun 2011;151(17):1105–8.
[22] Yuan H, Riley DC, Shen ZX, et al. Back-gated graphene anode for more efficient thermionic energy converters. Nano Energy 2017;32:67–72.
[23] Su S, Wang Y, Wang J, et al. Material optimum choices and parametric design strategies of a photon-enhanced solar cell hybrid system. Sol Energy Mater Sol Cells 2014;128:112–8.
[24] Buencuerpo J, Llorens JM, Zilio P, et al. Light-trapping in photon enhanced thermionic emitters. Opt Express 2015;23(19):A1220–35.
[25] Wang G, Chang B, Li X, et al. Solar energy conversion through thermally enhanced external photoelectric emission from NaCsSb photocathodes. Sol Energy Mater Sol Cells 2017;159:73–9.
[26] Martinelli RU. Thermionic emission from the Si/Cs/O (100) surface. J Appl Phys 1974;45(3):1183–90.
[27] Marshall AC. An equation for thermionic currents in vacuum energy conversion diodes. Appl Phys Lett 1998;73(20):2971–3.
[28] Musho TD, Paxton WF, Davidson JL, et al. Quantum simulation of thermionic emission from diamond films. J Vac Sci Technol, B 2013;31(2):021401.
[29] Zhuravlev AG, Romanov AS, Alperovich VL. Photon-enhanced thermionic emission from p-GaAs with nonequilibrium Cs overlayers. Appl Phys Lett 2014;105(25):251602.
[30] Kindig NB, Spicer WE. Band structure of cadmium sulfide—photoemission studies. Phys Rev 1965;138(2A):A561.
[31] Sahasrabuddhe K, Schwede JW, Bargatin I, et al. A model for emission yield from planar photocathodes based on photon-enhanced thermionic emission or negative-electron-affinity photoemission. J Appl Phys 2012;112(9):094907.
[32] Segev G, Rosenwaks Y, Kribus A. Loss mechanisms and back surface field effect in photon enhanced thermionic emission converters. J Appl Phys 2013;114(4):044505.
[33] Varpula A, Prunnila M. Diffusion-emission theory of photon enhanced thermionic emission solar energy harvesters. J Appl Phys 2012;112(4):044506.
[34] Schroder DK. Semiconductor material and device characterization. John Wiley & Sons; 2006.
[35] Su S, Wang Y, Liu T, et al. Space charge effects on the maximum efficiency and parametric design of a photon-enhanced thermionic solar cell. Sol Energy Mater Sol Cells 2014;121:137–43.
[36] Wang Y, Su S, Lin B, et al. Parametric design criteria of an irreversible vacuum thermionic generator. J Appl Phys 2013;114(5):053502.
[37] Olukunle OC, De DK. Thermo-electronic solar power conversion with a parabolic concentrator. J Semicond 2016;37(2):024002.
[38] Post AD, King BV, Kisi EH. Computational model and optimisation of a vacuum diode thermionic generator for application in concentrating solar thermal power. Appl Therm Eng 2017;117:245–53.
[39] Rufeh F. Performance improvement of cesium thermionic converters by addition of oxygen. In: 7th Intersociety energy conversion conference; 1972.
[40] Hansen LK, Hatch GL, Fitzpatrick GO, et al. The plasmatron as an advanced performance thermionic converter. In: 11th Intersociety energy conversion engineering conference; 1976, p. 1630–4.
[41] Shimada K. Low arc drop hybrid mode thermionic converter. In: 12th Intersociety energy conversion engineering conference; 1977, p. 1568–74.
[42] Henne R, Bradke MV, Weber W. Progress in the development of small flame heated thermionic energy converters. In: Intersociety energy conversion engineering conference, vol. 15; 1980, p. 2089–94.
[43] Goodale DB, Reagan P, Miskolczy G, et al. Combustion performance of CVD silicon carbide thermionic diodes. In: Energy to the 21st century; proceedings of the fifteenth intersociety energy conversion engineering conference; 1980, p. 2095–97.
[44] Smith MD, Manda ML, Britt EJ. Utilization of low temperature insulators and seals in thermionic converters. In: Energy to the 21st century; proceedings of the fifteenth intersociety energy conversion engineering conference; 1980, p. 2098–102.
[45] Stark G, Saunders M, Lieb D. Thermionic converter output as a function of collector temperature. In: Energy to the 21st century; Proceedings of the fifteenth intersociety energy conversion engineering conference; 1980, p. 2107–11.
[46] Goodale D, Lieb D, Neale D. Solar thermionic energy converter experiment. Proc, intersoc energy convers eng conf;(United States). Waltham, MA: Thermo Electron Corporation; 1982. 4(CONF-820814-).
[47] Dick RS, Britt EJ, Fitzpatrick GO, et al. High performance, close-spaced thermionic converters. Proc, intersoc energy convers eng conf.;(United States). Sunnyvale, California: Rasor Associates, Inc.; 1983. 1(CONF-830812-).
[48] El-Genk MS, Momozaki Y. An experimental investigation of the performance of a thermionic converter with planar molybdenum electrodes for low temperature applications. Energy Convers Manage 2002;43(7):911–36.
[49] Momozaki Y, El-Genk MS. Investigations of the performance of grooved electrodes thermionic converters at collector temperatures up to 1023K. Energy Convers Manage 2004;45(7):1153–73.
[50] Koeck FAM, Nemanich RJ. Substrate-diamond interface considerations for enhanced thermionic electron emission from nitrogen doped diamond films. J Appl Phys 2012;112(11):113707.
[51] Paramonov DV, El-Genk MS. A review of cesium thermionic converters with developed emitter surfaces. Energy Convers Manage 1997;38(6):533–49.
[52] Barabash MB, Busigin EP, Grigoryants VG, Yavor IP. Low voltage cesium arc in thermionic converter with extended cathode surface. Proceedings of the 2nd international conference on thermionic electrical power generation, Stresa, Italy; 1968.
[53] Busygin EP, Grigor'yants VG, Zhukov BG, et al. Possibility of determining the energy of a beam of slow electrons by a spectroscopic method. Teplofizika vysokikh temperatur 1970;8(3):657–9.
[54] Jensen KL, Lau YY, Jordan N. Emission nonuniformity due to profilimetry variation in thermionic cathodes. Appl Phys Lett 2006;88(16):164105.
[55] Zeng T. Thermionic-tunneling multilayer nanostructures for power generation.

Appl Phys Lett 2006;88(15):153104.
[56] Hutson AR. Velocity analysis of thermionic emission from single-crystal tungsten. Phys Rev 1955;98(4):889.
[57] Gardner FM, Girouard FE, Boeck WL, et al. Thermionic emission from single-crystal filaments. Surf Sci 1971;26(2):605–23.
[58] Kashetov A, Gorbatyi NA. Thermionic parameters of the faces of a rhenium crystal. Russ Phys J 1969;12(7):856–9.
[59] Culp Jr AW. Principles of energy conversion; 1991.
[60] Westover TL, Franklin AD, Cola BA, et al. Photo-and thermionic emission from potassium-intercalated carbon nanotube arrays. J Vacuum Sci Technol B, Nanotechnol Microelectron: Mater, Process, Meas, Phenomena 2010;28(2):423–34.
[61] Wei Y, Jiang K, Feng X, et al. Comparative studies of multiwalled carbon nanotube sheets before and after shrinking. Phys Rev B 2007;76(4):045423.
[62] Koeck FAM, Nemanich RJ. Low temperature onset for thermionic emitters based on nitrogen incorporated UNCD films. Diam Relat Mater 2009;18(2):232–4.
[63] Paxton WF, Howell M, Kang WP, et al. Influence of hydrogen on the thermionic electron emission from nitrogen-incorporated polycrystalline diamond films. J Vacuum Sci Technol B, Nanotechnol Microelectron: Mater, Process, Meas, Phenomena 2012;30(2):021202.
[64] Suzuki M, Ono T, Sakuma N, et al. Low-temperature thermionic emission from nitrogen-doped nanocrystalline diamond films on n-type Si grown by MPCVD. Diam Relat Mater 2009;18(10):1274–7.
[65] Koeck FAM, Nemanich RJ. Emission characterization from nitrogen-doped diamond with respect to energy conversion. Diamond Related Mater 2006;15(2):217–20.
[66] Kato H, Takeuchi D, Ogura M, et al. Heavily phosphorus-doped nano-crystalline diamond electrode for thermionic emission application. Diam Relat Mater 2016;63:165–8.
[67] Zhu F, Lin X, Liu P, et al. Heating graphene to incandescence and the measurement of its work function by the thermionic emission method. Nano Res 2014;7(4):553–60.
[68] Liang SJ, Ang LK. Electron thermionic emission from graphene and a thermionic energy converter. Phys Rev Appl 2015;3(1):014002.
[69] Silva SRP, Amaratunga GAJ, Okano K. Modeling of the electron field emission process in polycrystalline diamond and diamond-like carbon thin films. J Vacuum Sci Technol B: Microelectron Nanometer Struct Process, Meas, Phenomena 1999;17(2):557–61.
[70] Koeck FAM, Wang Y, Nemanich RJ. Thermionic converters based on nanostructured carbon materials. In: El-Genk MS, editor. AIP conference proceedings, vol. 813, no, 1, AIP; 2006, p. 607–13.
[71] Kataoka M, Zhu C, Koeck FAM, et al. Thermionic electron emission from nitrogen-doped homoepitaxial diamond. Diam Relat Mater 2010;19(2):110–3.
[72] Koeck FAM, Nemanich RJ, Lazea A, et al. Thermionic electron emission from low work-function phosphorus doped diamond films. Diamond Related Mater 2009;18(5):789–91.
[73] Loutfy RO, Samandi M, Moravsky A, et al. Carbon nanotubes as thermionic emitters. In: El-Genk MS, Bragg MJ, editors. AIP conference proceedings, vol. 699, no. 1, AIP; 2004, p. 773–80.
[74] Yaghoobi P, Vahdani Moghaddam M, Nojeh A. Solar electron source and thermionic solar cell. AIP Adv 2012;2(4):042139.
[75] Khoshaman AH, Koch AT, Chang M, et al. Nanostructured thermionics for conversion of light to electricity: simultaneous extraction of device parameters. IEEE Trans Nanotechnol 2015;14(4):624–32.
[76] Wei X, Golberg D, Chen Q, et al. Phonon-assisted electron emission from individual carbon nanotubes. Nano Lett 2010;11(2):734–9.
[77] Lee JH, Bargatin I, Melosh NA, et al. Optimal emitter-collector gap for thermionic energy converters. Appl Phys Lett 2012;100(17):173904.
[78] Narayanaswamy A, Shen S, Hu L, et al. Breakdown of the Planck blackbody radiation law at nanoscale gaps. Appl Phys A Mater Sci Process 2009;96(2):357–62.
[79] Khalid KAA, Leong TJ, Mohamed K. Review on Thermionic Energy Converters. IEEE Trans Electron Dev 2016;63(6):2231–41.
[80] Lee JH, Bargatin I, Gwinn TO, et al. Microfabricated silicon carbide thermionic energy converter for solar electricity generation. In: Micro electro mechanical systems (MEMS), 2012 IEEE 25th international conference on. IEEE, 2012, p. 1261–4.
[81] Rasor NS. Thermionic energy conversion plasmas. IEEE Trans Plasma Sci 1991;19(6):1191–208.
[82] Smith JR, Bilbro GL, Nemanich RJ. Theory of space charge limited regime of thermionic energy converter with negative electron affinity emitter. J Vacuum Sci Technol B: Microelectron Nanometer Struct Process, Meas, Phenomena 2009;27(3):1132–41.
[83] Smith JR, Bilbro GL, Nemanich RJ. Considerations for a high-performance thermionic energy conversion device based on a negative electron affinity emitter. Phys Rev B 2007;76(24):245327.
[84] Hassink G, Wanke R, Rastegar I, et al. Transparency of graphene for low-energy electrons measured in a vacuum-triode setup. APL Mater 2015;3(7):076106.
[85] Wanke R, Hassink GWJ, Stephanos C, et al. Magnetic-field-free thermoelectronic power conversion based on graphene and related two-dimensional materials. J Appl Phys 2016;119(24):244507.
[86] Koeck FAM, Nemanich RJ, Balasubramaniam Y, et al. Enhanced thermionic energy conversion and thermionic emission from doped diamond films through methane exposure. Diam Relat Mater 2011;20(8):1229–33.
[87] Ryan Smith J. Increasing the efficiency of a thermionic engine using a negative electron affinity collector. J Appl Phys 2013;114(16):164514.
[88] Fukuda R, Kasuga Y, Kato K, et al. Development of the oxygenated thermionic energy converters utilizing the sputtered metal oxides as a collector. In: Bragg MJ, El-Genk MS, editors. AIP conference proceedings, vol. 458, no. 1, AIP; 1999, p. 1444–51.
[89] El-Genk MS, Luke JR. Performance comparison of thermionic converters with smooth and macro-grooved electrodes. Energy Convers Manage 1999;40(3):319–34.
[90] Islam M, Inal OT, Luke JR. Development of electron reflection suppression materials for improved thermionic energy converter performance using thin film deposition techniques. J Appl Phys 2006;100(8):084903.
[91] Kribus A, Segev G. Solar energy conversion with photon-enhanced thermionic emission. J Opt 2016;18(7):073001.
[92] Takao H, Kobayashi K, Ito T. Ideal efficiency of photon-enhanced thermionic emission energy converter driven by blackbody radiation. Jpn J Appl Phys 2015;55(1):018003.
[93] Guo T. Negative electron affinity silicon heterojunction photocathodes with alkali antimonide intermediate layers. J Appl Phys 1992;72(9):4384–9.
[94] Spicer WE. Photoemissive, photoconductive, and optical absorption studies of alkali-antimony compounds. Phys Rev 1958;112(1):114.
[95] Varpula A, Tappura K, Prunnila M. Si, GaAs, and InP as cathode materials for photon-enhanced thermionic emission solar cells. Sol Energy Mater Sol Cells 2015;134:351–8.
[96] Reck K, Dionigi F, Hansen O. Photon-enhanced thermionic emission in cesiated p-type and n-type silicon. In: 29th European photovoltaic solar energy conference and exhibition; 2014, p. 328–330.
[97] Segev G, Rosenwaks Y, Kribus A. Efficiency of photon enhanced thermionic emission solar converters. Sol Energy Mater Sol Cells 2012;107:125–30.
[98] Su S, Zhang H, Chen X, et al. Parametric optimum design of a photon-enhanced thermionic solar cell. Sol Energy Mater Sol Cells 2013;117:219–24.
[99] Segev G, Weisman D, Rosenwaks Y, et al. Negative space charge effects in photon-enhanced thermionic emission solar converters. Appl Phys Lett 2015;107(1):013908.
[100] Wang Y, Liao T, Zhang Y, et al. Effects of nanoscale vacuum gap on photon-enhanced thermionic emission devices. J Appl Phys 2016;119(4):045106.
[101] Alabastri A, Toma A, Malerba M, et al. High temperature nanoplasmonics: the key role of nonlinear effects. ACS Photonics 2014;2(1):115–20.
[102] Edman Jonsson G, Fredriksson H, Sellappan R, et al. Nanostructures for enhanced light absorption in solar energy devices. Int J Photoenergy 2011;2011.
[103] Guler U, Boltasseva A, Shalaev VM. Refractory plasmonics. Science 2014;344(6181):263–4.
[104] Zhuravlev AG, Alperovich VL. Temperature dependence of photon-enhanced thermionic emission from GaAs surface with nonequilibrium Cs overlayers. Appl Surf Sci 2017;395:3–8.
[105] Sandovsky R, Segev G, Kribus A. Investigation of contact grid geometry for photon-enhanced thermionic emission (PETE) silicon based solar converters. Sol Energy 2016;133:259–73.
[106] Rosenwaks Y, Shapira Y, Huppert D. Metal reactivity effects on the surface recombination velocity at InP interfaces. Appl Phys Lett 1990;57(24):2552–4.
[107] Schwede JW, Sarmiento T, Narasimhan VK, et al. Photon-enhanced thermionic emission from heterostructures with low interface recombination. Nat Commun 2013;4:1576.
[108] Yang Y, Yang W, Sun C. Heterostructured cathode with graded bandgap window-layer for photon-enhanced thermionic emission solar energy converters. Sol Energy Mater Sol Cells 2015;132:410–7.
[109] Tang W, Yang W, Yang Y, et al. GaAs film for photon-enhanced thermionic emission solar harvesters. Mater Sci Semicond Process 2014;25:143–7.
[110] Liao T, Chen X, Lin B, et al. Performance evaluation and parametric optimum design of a vacuum thermionic solar cell. Appl Phys Lett 2016;108(3):033901.
[111] Ito T, Cappelli MA. Optically pumped cesium plasma neutralization of space charge in photon-enhanced thermionic energy converters. Appl Phys Lett 2012;101(21):213901.
[112] Bellucci A, Calvani P, Girolami M, et al. Optimization of black diamond films for solar energy conversion. Appl Surf Sci 2016;380:8–11.
[113] Calvani P, Bellucci A, Girolami M, et al. Black diamond for solar energy conversion. Carbon 2016;105:401–7.
[114] Sun T, Koeck FAM, Rezikyan A, et al. Photo induced electron emission from nitrogen doped diamond films on silicon. In: Vacuum nanoelectronics conference (IVNC), 2013 26th international. IEEE; 2013, p. 1–2.
[115] Sun T, Koeck FAM, Rezikyan A, et al. Thermally enhanced photoinduced electron emission from nitrogen-doped diamond films on silicon substrates. Phys Rev B 2014;90(12):121302.
[116] Girolami M, Criante L, Di Fonzo F, et al. Graphite distributed electrodes for diamond-based photon-enhanced thermionic emission solar cells. Carbon 2017;111:48–53.
[117] Neugebohrn N, Sun T, Koeck FAM, et al. Spatial correlation of photo-induced and thermionic electron emission from low work function diamond films. Diam Relat Mater 2013;40:12–6.
[118] Sun T, Koeck FAM, Stepanov PB, et al. Interface and interlayer barrier effects on photo-induced electron emission from low work function diamond films. Diam Relat Mater 2014;44:123–8.
[119] Sun T, Koeck FAM, Zhu C, et al. Combined visible light photo-emission and low temperature thermionic emission from nitrogen doped diamond films. Appl Phys Lett 2011;99(20):202101.
[120] Elfimchev S, Chandran M, Akhvlediani R, et al. Trap-assisted photon-enhanced thermionic emission from polycrystalline diamond films. Phys Status Solidi (a) 2015;212(11):2583–8.
[121] Sze SM, Ng KK. Physics of semiconductor devices. John wiley & sons; 2006.

[122] Polyakov VI, Rukovishnikov AI, Rossukanyi NM, et al. Charge-based deep level transient spectroscopy of undoped and nitrogen-doped ultrananocrystalline diamond films. Diamond Related Mater 2003;12(10):1776–82.
[123] Bellucci A, Calvani P, Girolami M, et al. Defect engineering of diamond cathodes for high temperature solar cells. In: Environment and electrical engineering (EEEIC), 2015 IEEE 15th international conference on. IEEE; 2015, p. 1616–19.
[124] Nemanič V, Žumer M, Kovač J, et al. In situ reactivation of low-temperature thermionic electron emission from nitrogen doped diamond films by hydrogen exposure. Diam Relat Mater 2014;50:151–6.
[125] Yang Y, Yang W, Tang W, et al. High-temperature solar cell for concentrated solar-power hybrid systems. Appl Phys Lett 2013;103(8):083902.
[126] Yang Y, Yang W, Sun C. Diffusion emission model for solid-state photon-enhanced thermionic emission solar energy converters. Mater Sci Semicond Process 2015;35:120–6.
[127] Bian Z, Shakouri A. Enhanced solid-state thermionic emission in nonplanar heterostructures. Appl Phys Lett 2006;88(1):012102.
[128] Su S, Chen X, Liao T, et al. Photon-enhanced electron tunneling solar cells. Energy 2016;111:52–6.
[129] Moizhes B Y. Effectiveness of low-temperature thermionic converters for topping the Rankine cycle. SAE technical paper; 1992.
[130] Paramonov DV, Carelli MD. A thermionic topping cycle for advanced gas turbines. In: Proc 33rd IECEC, American Nuclear Society, Chicago, vol.72; 1998, p. 1962–67.
[131] Miskolczy G, Wang CC, Lieb DP, et al. Thermionic combustor application to combined gas and steam turbine power plants. In: 16th Intersociety energy conversion engineering conference, vol. 1; 1981, p. 1956–61.
[132] Allen DT, Nikolaev YV, Eryomin SA, et al. Applications of out-of-core close-spaced thermionics. In: El-Genk MS, Hoover MD, editors. AIP conference proceedings, vol. 271, no. 3, AIP; 1993, p. 1241–9.
[133] Datas A. Hybrid thermionic-photovoltaic converter. Appl Phys Lett 2016;108(14):143503.
[134] Fitzpatrick GO, Britt EJ, Carnasciali G. Increased central station power plant efficiency with a thermionic topping system. In: 12th intersociety energy conversion engineering conference, vol. 1; 1977, p. 1602–9.
[135] Fitzpatrick GO, Allen DT. Cascaded thermionic converters applied to space nuclear power systems. In: El-Genk MS, Hoover MD, editors. AIP conference proceedings, vol. 301, no. 1, AIP; 1994, p. 819–27.
[136] Miskolezy G, Morgan D, Turner R. Design and economic evaluation of thermionic cogeneration in a chlorine-caustic plant; 1985.
[137] Ender AY, Kolyshkin IN, Kuznetsov VI, et al. Cascaded space solar power system with high temperature Cs-Ba thermionic converter and AMTEC. In: El-Genk MS, Bragg MJ, editors. AIP conference proceedings, vol. 420, no. 1, AIP; 1998, p. 1565–70.
[138] Wang Y, Su S, Liu T, et al. Performance evaluation and parametric optimum design of an updated thermionic-thermoelectric generator hybrid system. Energy 2015;90:1575–83.
[139] Xuan XC, Li D. Optimization of a combined thermionic–thermoelectric generator. J Power Sources 2003;115(1):167–70.
[140] Huang C, Pan Y, Wang Y, et al. An efficient hybrid system using a thermionic generator to harvest waste heat from a reforming molten carbonate fuel cell. Energy Convers Manage 2016;121:186–93.
[141] Melosh N. Combined conversion of heat and light with Photon Enhanced Thermionic Emission for solar energy harvesting. In: APS meeting abstracts; 2012.
[142] Segev G, Kribus A, Rosenwaks Y. High performance isothermal photo-thermionic solar converters. Sol Energy Mater Sol Cells 2013;113:114–23.
[143] Reck K, Hansen O. Thermodynamics of photon-enhanced thermionic emission solar cells. Appl Phys Lett 2014;104(2):023902.
[144] Segev G, Rosenwaks Y, Kribus A. Limit of efficiency for photon-enhanced thermionic emission vs. photovoltaic and thermal conversion. Sol Energy Mater Sol Cells 2015;140:464–76.
[145] Imenes AG, Mills DR. Spectral beam splitting technology for increased conversion efficiency in solar concentrating systems: a review. Sol Energy Mater Sol Cells 2004;84(1):19–69.
[146] Mojiri A, Taylor R, Thomsen E, et al. Spectral beam splitting for efficient conversion of solar energy—A review. Renew Sustain Energy Rev 2013;28:654–63.
[147] Sun T, Koeck FAM, Rezikyan A, et al. Photo induced electron emission from nitrogen doped diamond films on silicon. In: Vacuum nanoelectronics conference (IVNC), 2013 26th international. IEEE; 2013, p. 1–2.
[148] Segev G, Rosenwaks Y, Kribus A. Single bandgap solar converters unbounded by the Shockley Queisser limit. In: Dimroth F, Araki K, Antón I, editors. AIP conference proceedings, vol. 1556, no. 1, AIP; 2013, p. 53–6.
[149] Nemanich R. Diamond based isothermal photon-enhanced thermionic solar energy conversion topping devices; 2014.
[150] Council N. Thermionics quo vadis? An assessment of the DTRA's advanced thermionics research and development program; 2001.
[151] Hsieh TM, Phillips WM. An improved thermionic power conversion system for space propulsion; 1978.
[152] Shimada K, Swerdling M. Solar thermionic power systems for terrestrial applications. In: 12th Intersociety energy conversion engineering conference; 1977, p. 1590–601.
[153] Barlev D, Vidu R, Stroeve P. Innovation in concentrated solar power. Sol Energy Mater Sol Cells 2011;95(10):2703–25.
[154] Xie WT, Dai YJ, Wang RZ, et al. Concentrated solar energy applications using Fresnel lenses: A review. Renew Sustain Energy Rev 2011;15(6):2588–606.
[155] Han YM, Wang RZ, Dai YJ, et al. Studies on the light permeance characteristic of a Fresnel lens group applied in high concentration solar energy. J Opt A: Pure Appl Opt 2007;9(11):988.
[156] Zhang HL, Baeyens J, Degrève J, et al. Concentrated solar power plants: Review and design methodology. Renew Sustain Energy Rev 2013;22:466–81.
[157] McVey JB, Britt EJ, Fitzpatrick GO, et al. The design of series-parallel connected thermionic converter arrays. In: 16th Intersociety energy conversion engineering conference; 1981, p. 1968–73.
[158] Kongtragool B, Wongwises S. A review of solar-powered Stirling engines and low temperature differential Stirling engines. Renew Sustain Energy Rev 2003;7(2):131–54.
[159] Ni M, Shi B, Xiao G, et al. Improved simple analytical model and experimental study of a 100 W β-type stirling engine. Appl Energy 2016;169:768–87.
[160] Chen H, Goswami DY, Stefanakos EK. A review of thermodynamic cycles and working fluids for the conversion of low-grade heat. Renew Sustain Energy Rev 2010;14(9):3059–67.
[161] Tchanche BF, Lambrinos G, Frangoudakis A, et al. Low-grade heat conversion into power using organic Rankine cycles–A review of various applications. Renew Sustain Energy Rev 2011;15(8):3963–79.
[162] Garg P, Kumar P, Srinivasan K. Supercritical carbon dioxide Brayton cycle for concentrated solar power. J Supercrit Fluids 2013;76:54–60.
[163] Mints P. Photovoltaic industry price behavior 1975 through 2015, drivers, patterns and outcomes. In: Photovoltaic specialists conference (PVSC), 2016 IEEE 43rd. IEEE; 2016, p. 3331–4.
[164] Fitzpatrick GO, Britt EJ, Moyzhes B. Updated perspective on the potential for thermionic conversion to meet 21st century energy needs. In: Energy conversion engineering conference, 1997. IECEC-97., Proceedings of the 32nd intersociety. IEEE; 1997, p. 1045–51.
[165] Wu C. Optimal power from a radiating solar-powered thermionic engine. Energy Convers Manage 1992;33(4):279–82.
[166] Moyzhes BY, Geballe TH. The thermionic energy converter as a topping cycle for more efficient heat engines—new triode designs with a longitudinal magnetic field. J Phys D Appl Phys 2005;38(5):782.
[167] Marx K, Bolhàr-Nordenkampf J, Pröll T, et al. Chemical looping combustion for power generation—Concept study for a 10 MW th demonstration plant. Int J Greenhouse Gas Control 2011;5(5):1199–205.
[168] Cong CE, Velautham S, Darus AN. Solar thermal Organic Rankine Cycle as a renewable energy option. J Mekanikal 2005;20:68–77.